# Trimodal Therapy: Combining Hyperthermia with Repurposed Bexarotene and Ultrasound for Treating Liver Cancer

Santosh K. Misra,[†] Goutam Ghoshal,[‡] Manas R. Gartia,[†,■] Zhe Wu,[§,■] Arun K. De,[∥,■] Mao Ye,[†,■] Corinne R. Bromfield,[⊥] Emery M. Williams,[‡] Kuldeep Singh,[#] Krishnarao V. Tangella,[¶] Laurie Rund,[∥] Klaus Schulten,[§,▲] Lawrence B. Schook,[†,∥] Partha S. Ray,[†,▲] Everette C. Burdette,[*,‡] and Dipanjan Pan[*,†,▲,□,▽]

[†]Department of Bioengineering, [§]Center for the Physics of Living Cells, Department of Physics, [∥]Department of Animal Sciences, [⊥]Agricultural Animal Care and Use Program, [#]Veterinary Diagnostic Laboratory, [¶]Pathology and Internal Medicine, [▲]Beckman Institute of Advanced Science and Technology, and [▽]Department of Materials Science and Engineering, University of Illinois at Urbana—Champaign, Champaign, Illinois 61820, United States, [‡]Acoustic Med System, 208 Burwash Avenue, Savoy, Illinois 61874, United States, and [□]Mills Breast Cancer Institute, Carle Foundation Hospital, 502 North Busey, Urbana, Illinois 61801, United States. [■]M.R.G., Z.W., A.K.D., and M.Y. contributed equally.

**ABSTRACT** Repurposing of existing cancer drugs to overcome their physical limitations, such as insolubility, represents an attractive strategy to achieve enhanced therapeutic efficacy and broaden the range of clinical applications. Such an approach also promises to offer substantial cost savings in drug development efforts. Here we repurposed FDA-approved topical agent bexarotene (Targretin), currently in limited use for cutaneous manifestations of T-cell lymphomas, and re-engineer it for use in solid tumor applications by forming self-assembling nanobubbles. Physico-chemical characterization studies of the novel prodrug nanobubbles demonstrated their stability, enhanced target cell internalization capability, and highly controlled release profile in response to application of focused ultrasound energy. Using an *in vitro* model of hepatocellular carcinoma and an *in vivo* large animal model of liver ablation, we demonstrate the effectiveness of bexarotene prodrug nanobubbles when used in conjunction with catheter-based ultrasound, thereby highlighting the therapeutic promise of this trimodal approach.

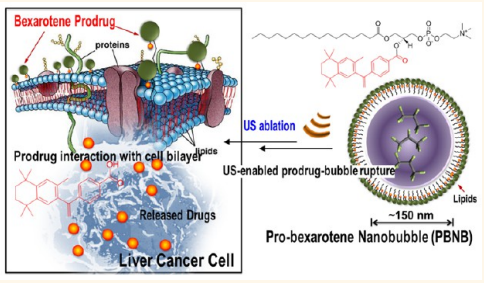


**KEYWORDS:** liver cancer · thermal ablation · anticancer prodrug nanobubble · drug repurposing

American Cancer Society estimated that in 2015 approximately 1.66 million new cancer cases are expected to be diagnosed in the United States.[1] A brand-new drug for treating cancer through a conventional drug discovery pipeline is time-consuming and expensive. One solution is to repurpose drugs. In this process, a therapeutic agent that is approved to treat one type of disease or condition is re-examined for treating other diseases. Bexarotene (4-[1-(5,6,7,8-tetrahydro-3,5,5,8,8-pentamethyl-2-naphthalenyl)ethenyl]benzoic acid, Targretin) is an FDA-approved drug, currently in limited use for cutaneous manifestations of T-cell lymphomas (CTCL).[2] It is a known orphan nuclear agonist and a member of a subclass of retinoids that selectively activate retinoid X receptors (RXRs).[3] These retinoid receptors have biologic activity distinct from that of retinoic acid receptors (RARs). Bexarotene selectively binds and activates retinoid X receptor subtypes (RXR$\alpha$, RXR$\beta$, RXR$\gamma$). RXRs can form heterodimers with various receptor partners such as thyroid receptor, vitamin D receptor, RARs, and peroxisome proliferator activator receptors (PPARs).[4] Once activated, these receptors function as transcription factors that regulate the expression of genes that control cellular differentiation and proliferation.[4] Despite being clinically approved, the use of this agent is only limited to topical application primarily due to the poor solubility of the agent, dose-limiting toxicities, or lack of objective responses. We hypothesize that a re-engineered form of the drug will be more effective for treating primary

* Address correspondence to dipanjan@illinois.edu, clifb@acousticmed.com.

Received for review April 5, 2015 and accepted October 4, 2015.

**Published online October 05, 2015**
10.1021/acsnano.5b05974

and secondary hepatocellular carcinoma. Liver is a common site of metastasis from many gastrointestinal and extra gastrointestinal primary cancers, including breast, lung, esophagus, stomach, pancreas, kidney, and melanoma.[5−8] The recent developments of minimally or noninvasive techniques to treat liver cancer provides quick recovery, less risk of wound infection, and less pain. Cryo-ablation,[9,10] radio frequency,[11−14] microwave heating,[15−17] and high-intensity focused ultrasound (HIFU)[18−23] are examples of minimally invasive thermal therapies that are under investigation, with several of these techniques now used in patients. Ultrasound (US) is a promising noninvasive approach for treating cancer through thermal ablation or hyperthermia. The use of ultrasound to treat tumors has been investigated in prostate,[19,20,24] liver,[18,22,25−27] kidney,[28] brain,[29,30] and eye conditions.[31,32] However, current systems remain highly dependent on operator skill and cannot treat many tumors because there is insufficient control of the size and shape of the zone of necrosis and little/no control over ablator trajectory within tissue and often take long treatment time. Remedying these problems requires advances in end-effector design, robust image guidance, and precise steering of the ablator device to the desired target location. Here we develop a catheter-based ultrasound therapeutic device with spatially tracked 3D ultrasound imaging and deliver the drug in combination with targeted drug payload using the pro-bexarotene nanobubble (PBNB) under therapeutic ultrasound exposure (Figure 1).

## RESULTS AND DISCUSSION

**Synthesis of Pro-bexarotene.** We synthesize and characterize the prodrug version of bexarotene (denoted as pro-bexarotene). In this procedure, 1-palmitoyl-2-hydroxy-*sn*-glycero-3-phosphocholine (16:0 Lyso-PC) (24.8 mg, 0.05 mmol), ethylene dichloride (19.1 mg, 0.1 mmol), and dimethylaminopyridine (catalytic amount) were mixed in anhydrous $CHCl_3$ solution (1 mL) and stirred for 15 min at ambient temperature. To this mixture we added bexarotene (17.4 mg, 0.05 mmol dissolved in 0.5 mL of anhydrous $CHCl_3$) and stirred for 24 h at room temperature. The completion of the reaction was monitored by thin layer chromatography (silica). The resultant organic solution was then washed several times with water and extracted with excess dichloromethane. Dichloromethane was evaporated under reduced pressure to afford 23.1 mg of compound in 56% yield as a light yellow solid (Scheme S1). NMR and mass studies were used to characterize the solid. $^1$H NMR ($CDCl_3$, 400 MHz): $\delta$ 7.93 (d, $J$ = 8.0 Hz, 2H), 7.32 (d, $J$ = 8.0 Hz, 2H), 7.10 (s, 1H), 7.06 (s, 1H), 5.78 (s, 1H), 5.30 (s, 1H), 4.35 (q, $J$ = 4.0 Hz, 2H), 3.89 (s, 2H), 3.22 (s, 4H), 2.30 (s, 2H), 1.93 (s, 4H), 1.68 (s, 6H), 1.53 (s, 3H), 1.36 (m, 6H), 1.69 (m, 12H), 1.23 (m, 24H), 0.85 (m, 3H). HRMS calcd for $C_{48}H_{76}NO_8P$ $m/z$: 826.5394 $(MH)^+$; found, 826.5387.

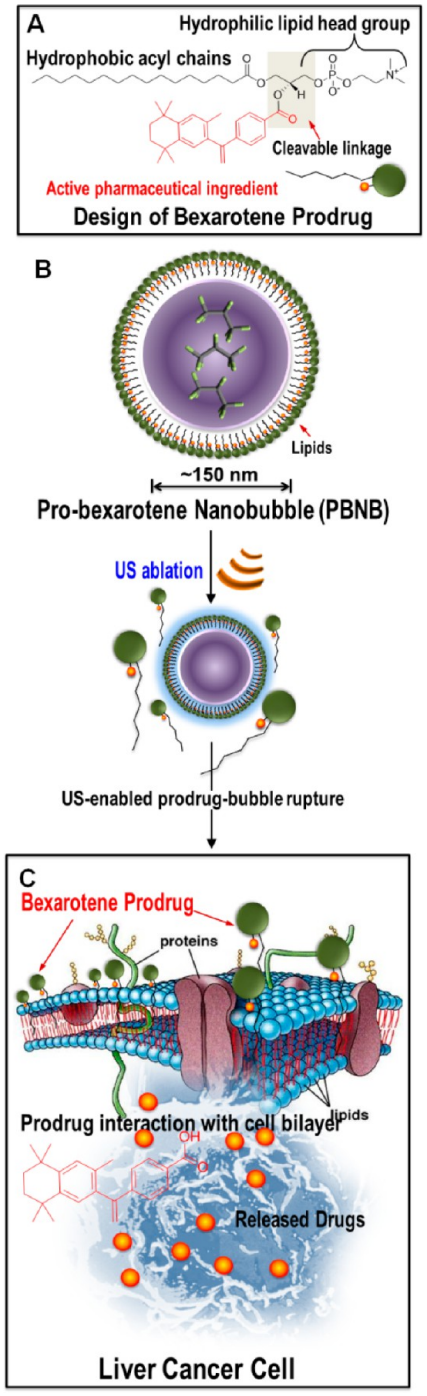


**Figure 1. Overall design of repurposed therapeutics. (A) Design of bexarotene prodrug and its chemical components; (B) layered arrangement of bexarotene prodrug after self-assembling into a gas-filled bubble followed by its rupture upon US exposure; (C) prodrug interacts favorably with the cancer cell membrane to get inserted and eventually be cleaved enzymatically, releasing the active pharmaceutical ingredient.**

**Susceptibility of Pro-bexarotene toward Enzyme and pH.** We determined whether the pro-bexarotene can be degraded in the presence of enzyme and acidic pH. The prodrug (500 $\mu$L) was incubated for 2 h with 0.278 mg ($3.36 \times 10^{-7}$ mol) of phospholipase A2 or

acidic pH (4.1). The samples were continuously agitated on a nutator to prevent settling. The mixture was isolated and analyzed by HRMS to observe signature peaks of cleaved and liberated bexarotene. High-resolution mass spectrometry (HRMS) confirmed the release of bexarotene from the prodrug under enzymatic or low pH condition.

**Density Functional Theory (DFT) Study.** DFT calculations were performed on bexarotene, 1-palmitoyl-2-hydroxy-*sn*-glycero-3-phosphocholine (Lyso-PC), octafluoropropane ($C_3F_8$), and pro-bexarotene. This technique enabled the analysis of electronic distribution and feasibility of forming nanoassemblies and prediction of the pharmacological activities. The pharmacological activities of drugs are affected by the electronic distribution on the drug molecules.[33−36] The reactivity of a molecule, for example, intermolecular interaction, is controlled by the frontier molecular orbitals (FMO) such as highest occupied molecular orbitals (HOMO) and the lowest unoccupied molecular orbitals (LUMO). The HOMO energy indicates the region of molecules, which can donate electrons during the complex formation with proteins or other receptor molecules. The LUMO energy region signifies the site of the molecules which can accept electrons from the protein (or other molecules) during interaction.[37] In a drug−receptor system, the HOMO state of the drugs generally interacts with the LUMO state of the receptor and the LUMO state of the drugs interacts with the HOMO state of the receptor.[37] The energy gap (HOMO−LUMO gap) is inversely proportional to the activity of the drugs.[37] Hence, the drug with the smallest energy band gap between the HOMO and LUMO is the most active and typically exhibits the highest cytotoxic activity. Similarly, a larger energy band gap leads to greater stabilization and binding with a receptor. The DFT calculation predicts that the Lyso-PC will be least cytotoxic. Comparing the prodrug and drug, the calculation predicts the prodrug to be less cytotoxic (as prodrug $\Delta E$ is larger than that of the drug; refer to Table 1) and more stable than the drug.

Figure 2 shows the plot of the HOMO and LUMO of the prodrug and its components showing the main atomic contribution of the orbitals. The electron-rich center is shown in red, while the electron-poor center is shown in blue in the HOMO plot. The region with high electron density (red) can be regarded as preferred nucleophilic centers, and regions with low electron density (blue) are potential electrophilic sites. For Lyso-PC and pro-bexarotene, most of the electron density is concentrated near the phosphodiester bond, making it a hydrophilic end. There is little change in the electron density distribution on Lyso and pro-bexarotene, indicating that the Lyso-PC structural properties remain intact even after the drug insertion. The LUMO of the drug (bexarotene) showed electron-deficient centers near the phenyl ring. Therefore, for the HOMO−1 energy level, the electron density of pro-bexarotene is pushed toward the phenyl ring (Figure 2), creating a curvature of the membrane compared to that without drug (Lyso-PC). This may suggest that the probability of

**TABLE 1. Energies of Both HOMO and LUMO and Their Gaps (in eV) Calculated for Prodrug and Its Components**

| compound | $E_{HOMO}$ (eV) | $E_{LUMO}$ (eV) | $\Delta E$ |
|---|---|---|---|
| Lyso-PC | −4.731 | −1.406 | 3.325 |
| pro-bexarotene | −4.708 | −1.822 | 2.886 |
| bexarotene | −6.174 | −3.518 | 2.656 |

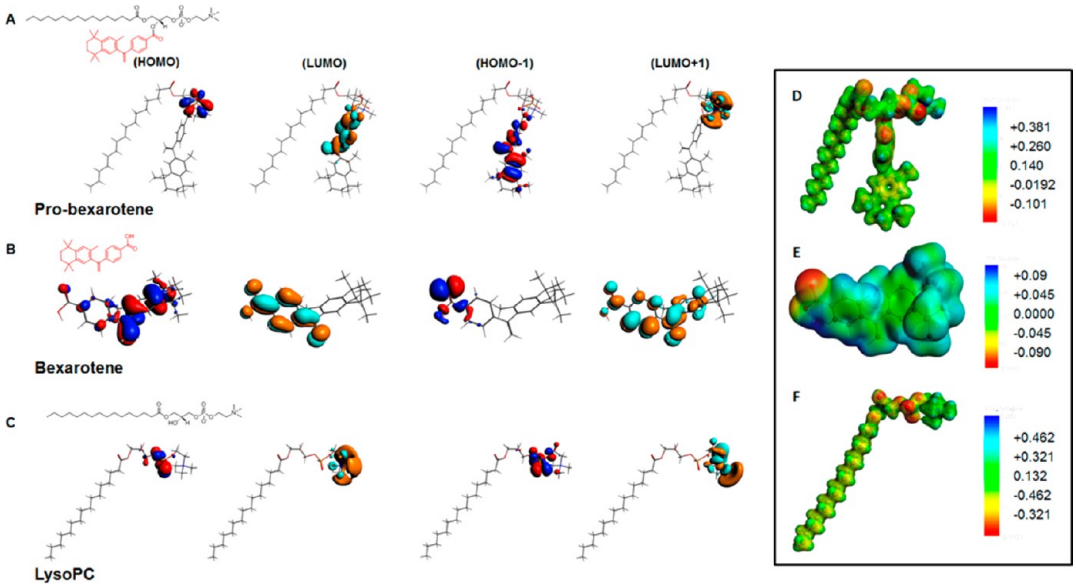


**Figure 2. Density functional theory distributions of (A) pro-bexarotene, (B) bexarotene, and (C) Lyso-PC and molecular electrostatic potentials of (D) pro-bexarotene, (E) bexarotene, and (F) Lyso-PC.**

**TABLE 2. Electrical Properties of the Drug and Prodrug**

| | polarizability | | | | | |
|---|---|---|---|---|---|---|
| | $\alpha_{xx}$ | $\alpha_{yy}$ | $\alpha_{zz}$ | average polarizability | dipole moment, $\mu$ (debye) | dipole length (e Bohr) |
| bexarotene | 230.16 | 270.11 | 382.31 | 294.2 | 7.72 | 3.037 |
| pro-bexarotene | 642.62 | 831.18 | 648.32 | 707.37 | 14.55 | 5.725 |

forming a nanoassembly is higher for pro-bexarotene than for Lyso-PC alone, as seen in our experiments. The HOMO molecular orbital of pro-bexarotene is mainly located near the phosphodiester bond, indicating the existence of a possible reactive site. Therefore, electrophilic attacks might take place on these sites. On the other hand, the LUMO of pro-bexarotene is primarily concentrated on the phenyl ring of the drug end of bexarotene. Therefore, the negatively charged polar residues of the receptor are more favorable on these sites (Table 1).

Further, comparing the dipole moment of pro-bexarotene, bexarotene, and Lyso-PC revealed the compound with higher propensity to form a nanoassembly and to interact with the cell membrane. It is generally understood that the compound with the largest dipole moment and larger dipole polarizability will have higher activity[38] (Table 2).

In order to further understand the activity of pro-bexarotene, we compared the molecular electrostatic potentials (MEPs) of pro-bexarotene and its components (Figure 2D–F). Previously, MEP had been utilized to understand the potency of carbinolamine analogues in the antimalarial drugs,[39] LpxC inhibition activity of 2-aryloxazolines, aroylserines, and 2-arylthiazolines,[40] 17b-aminoestrogen anticoagulant effect,[36] and aurora A/B kinase inhibitor activity.[37] Comparing the MEP shows that the pro-bexarotene compound has an increased negative charge region (in red) located near the phosphodiester bond and Lyso-PC–drug junction. Most of the positive charges (shown in blue) reside on hydrogen atom in the trimethylamine region. This may indicate the site from where the electrons are being pulled away by strongly withdrawing substituents. This may create a hydrophobic end (electron-deficient site) and contribute to the directional transport within the lipid bilayer membranes.[41] As shown in Table 2, in addition to the geometrical parameters and charge distribution, we calculated the polarizability and dipole moment of the drug and prodrug. These properties are quite useful in describing the quantitative structure property and structure–activity relationship of the compound under study.[37,42,43] The higher average polarizability and dipole moment of the prodrug compared to that of the drug signifies the better activity and higher potency of the prodrug. The static polarizability of bexarotene is highest along the *zz* direction, whereas for pro-bexarotene, it is highest along the *yy* direction. The directional dependence of polarizability reveals the possible dipole–dipole interaction between the target molecule and the drug/prodrug. This may possibly contribute to the different interaction probability of PBNB on the cell surface depending on the symmetry of cell surface ligands.

**Preparation and Physico-chemical Characterizations of Pro-bexarotene Nanobubbles and Controls.** Pro-bexarotene molecules were used to prepare pro-bexarotene NPs *via* a membrane hydration method.[44] The synthetic system requires[45] $C_3F_8$ gas purging with simultaneous bath sonication to prepare PBNB from pro-bexarotene NPs. Respective control lipid nanobubbles were also prepared NBs without the utilization of pro-bexarotene. As-synthesized PBNBs were evaluated for their physicochemical integrity before and after US exposure. It was found that the size of PBNB ($160 \pm 20$ nm) decreased ($80 \pm 10$ nm) on exposure to US, while in the case of NBs, size decreased from $200 \pm 20$ to $170 \pm 10$ nm only (Figure 3A,B). The surface potential of PBNB changed from $-29 \pm 1$ to $-34 \pm 2$ on US exposure, while for NBs, it changed from $-22 \pm 1$ to $-25 \pm 1$ (Figure 3C). The variation of surface charge potential upon US exposure is possibly due to an effect of the reassembly process of the amphiphilic prodrug. The presence of a higher negative electrophoretic potential also supports the successful lipid coating around these particles.

The morphological distribution of PBNB in the anhydrous state was studied by transmission electron microscopy (TEM). Negatively stained (0.4% uranyl acetate) pro-bexarotene NP and PBNB samples were compared for their morphological distributions and variations. The anhydrous state diameter of the pro-bexarotene NP was found to be $70 \pm 20$ nm, while the size of PBNB was $90 \pm 10$ nm (Figure 3D,E). A slight increase in the particle diameter is the result of expansion of the outer layer of assembled pro-bexarotene molecules due to a volume expansion by the insertion of gaseous $C_3F_8$.

X-ray diffraction (XRD) studies were performed to verify the US-exposure-mediated disruption of PBNB. Pro-bexarotene NPs showed ordered-ness with a peak at $2\theta$ value of 11.5 and was retained even in the form of PBNB, but US exposure decimated the ordered-ness peak; a peak at $2\theta$ value of 10.8 represents the crystallinity peak due to sodium phosphate salt from Dulbecco's phosphate buffer (Figure 3F). This demonstrates the loss of pro-bexarotene molecule assembly due to the application of US.

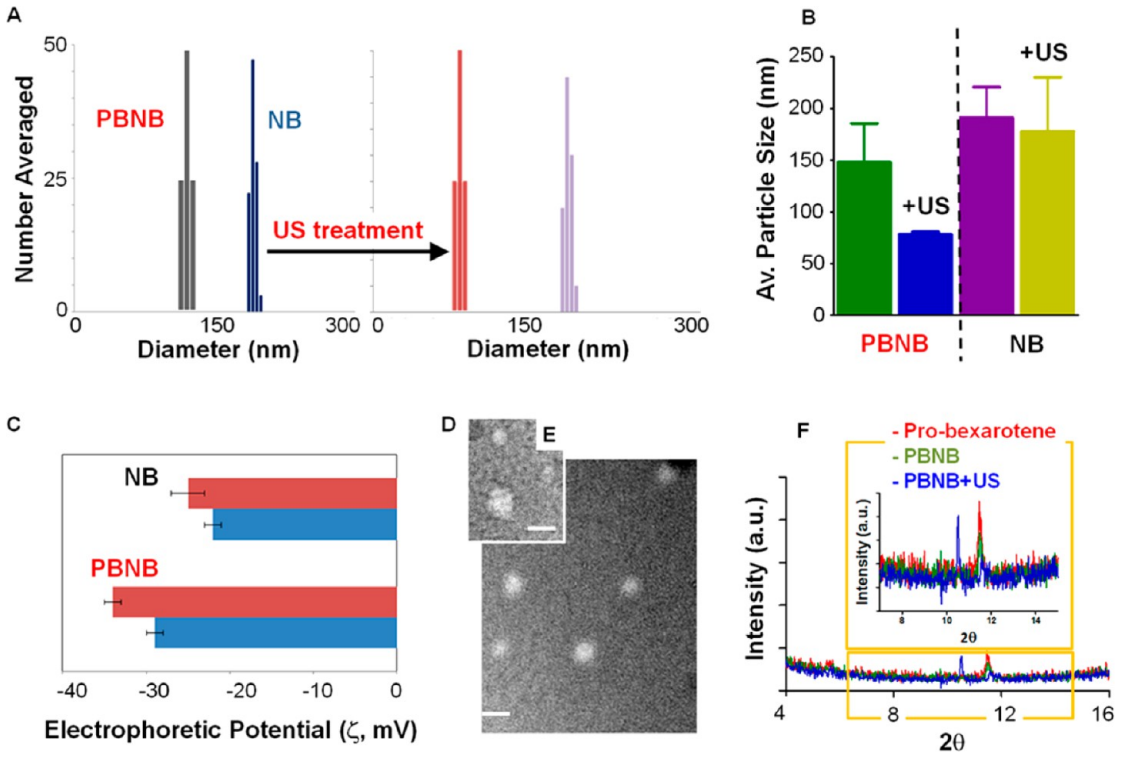


**Figure 3. Physico-chemical characterization of PBNB and effect of US exposure. (A) Bar diagrams of change in hydrodynamic diameter of PBNBs and NBs after US exposure. (B) Comparison of average particle size variation obtained from three independent experiments. (C) ζ-Potential distribution. Anhydrous state morphology of (D) PBNB and (E) pro-bexarotene NPs. (F) X-ray diffraction patterns of pro-bexarotene NPs, PBNB, and PBNB+US.**

Raman spectroscopic analyses of individual components of PBNBs were measured and found to be significantly distinguishable (Figure 4A). Raman peaks from bexarotene (782, 1288, and 1606 $cm^{-1}$) were nonoverlapping with 717, 873, 1062, 1098, 1128, 1295, 1437, and 2890 $cm^{-1}$ peaks from the lipid molecule, which were found to be coexisting as 1606 and 2890 $cm^{-1}$ in the case of pro-bexarotene. The peak at 1606 $cm^{-1}$, which is assigned to C═C backbone stretching of bexarotene, can be found in both bexarotene and pro-bexarotene. This shows that the preparation of prodrug reserved the crystalline state and chemical properties of bexarotene. The symmetric CH stretching mode at 2890 $cm^{-1}$ observed for lipid and pro-bexarotene gives evidence that bexarotene is conjugated to the lipid in pro-bexarotene. Figure 4B shows the effect of US on PBNB. A significant change was noticed when PBNB was exposed to US. For example, the peak at 968 $cm^{-1}$ (CH out-of-plane vibration of bexarotene) became stronger after US exposure. The peaks at 1606 $cm^{-1}$ (C═C vibration) and 483 $cm^{-1}$ (CH rocking vibration near the P atom of the lipid) were diminished after US exposure to PBNB (Figure 4B).

In order to gain insight into the fate of PBNB, pre- and post-US exposure, Raman spectroscopic measurements were performed on bexarotene, lipid, pro-bexarotene, PBNB, and NB. Figure 4C,D shows the optical images (5× magnification) of PBNB samples before and after US exposure, respectively. The figures clearly show a dramatic change in morphology after US exposure, revealing a thin spread of lipid molecules (Figure 4D). Findings from the Raman experiment further corroborated the XRD result, demonstrating the loss of arrangements of pro-bexarotene molecules in PBNBs after US exposure (Figure 3F). Similar changes were also observed for NB samples after US exposure (Figure S2A,B).

Presumably, US exposure to PBNBs changes the orientation of lipidic tail and enables the CH out-of-plane vibrational mode of the drug (bexarotene). The control (NB) did not show any such changes after exposure to US (Figure S2B). Raman studies strongly support the conversion of pro-bexarotenes to PBNBs and assembly-disruptive effects of US exposure. Additional DFT studies were performed to further confirm the respective signature peaks for individual components of PBNB and controls (Figure 4E,F).

**Molecular Dynamics Simulations and Fate of PBNBs after US Exposure.** After establishing that PBNB can be prepared stably, we performed molecular dynamics simulations to visualize the interaction of pro-bexarotene with the cell surface and internalization with the cellular membranes (Figure 5). A very strong cell uptake for the prodrug was observed. We performed molecular dynamics simulation in full atomic detail to model the insertion of the prodrug into a membrane bilayer. Initially, the prodrug molecule was placed 5 Å above the membrane and solvated by water. After ~60 ns, the

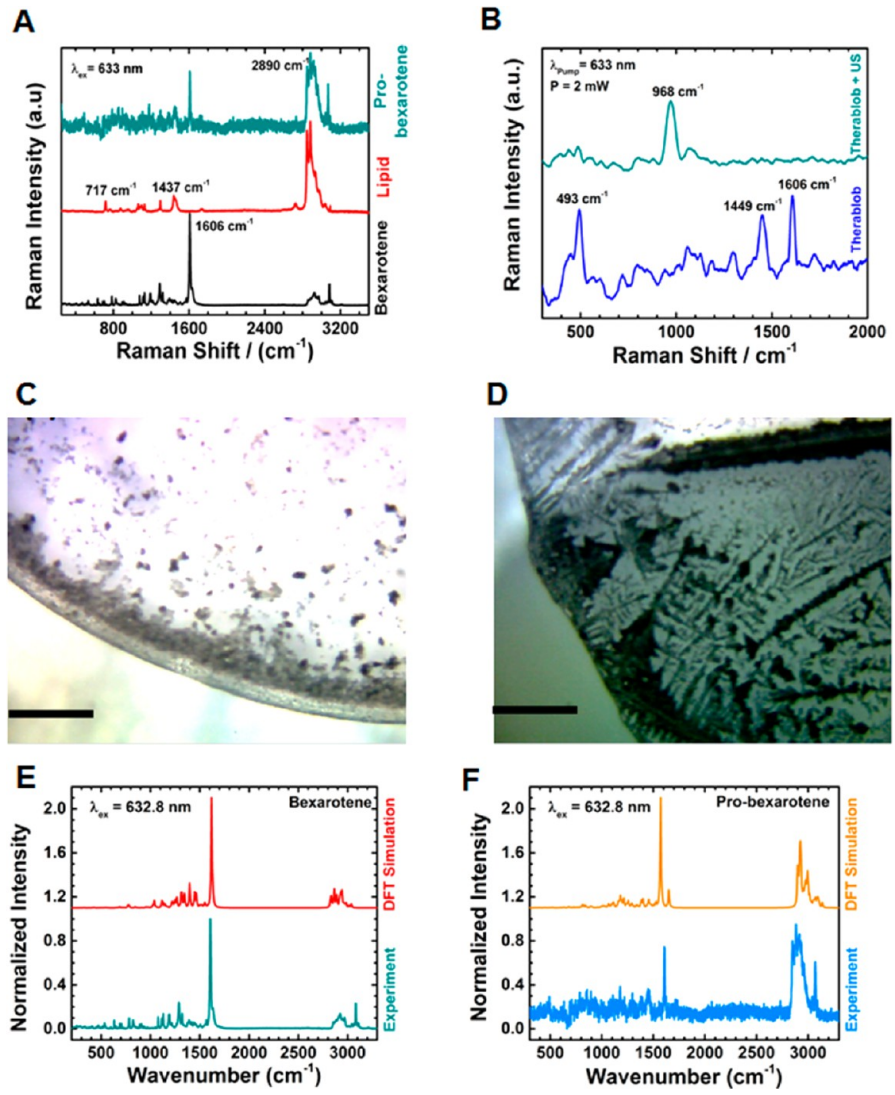


**Figure 4. Raman scattering patterns of (A) bexarotene, Lyso-PC, and pro-bexarotene in powdered form. (B) PBNB before and after US exposure. Raman imaging of PBNB (C) before and (D) after US exposure (scale bar 200 $\mu$m; 5×). DFT-simulated Raman scattering patterns compared with experimental Raman spectra for (E) bexarotene and (F) pro-bexarotene.**

prodrug starts to insert its Lyso-PC hydrocarbon tail into the membrane. Within the next 5 ns, the PC hydrocarbon tail goes deeper into the membrane's hydrophobic core, bringing along the aromatic group of the prodrug. The PC headgroup aligns with the membrane headgroup, and the whole prodrug molecule behaves similarly as a lipid molecule. After the insertion process, the prodrug stays in the membrane for the rest of the simulation (400 ns). For a dynamic simulated membrane entry process, please see Supporting Information movies derived from NAMD[54,63,64] simulations of pro-bexarotene and a lipid bilayer (movie 20).

Observed from the simulation, the Lyso-PC hydrocarbon tail interacts favorably with the membrane hydrophobic core and thus facilitates the prodrug membrane insertion. The bexarotene group, however, prefers regions slightly below the membrane−water interface, that is, regions close to the lipid glycerol group, similar to aromatic amino acid side chains such as phenylalanine and tryptophan.[46] Based on the potential of mean force calculations, the membrane insertion free energy of the bexarotene group in the prodrug is −19.8 ± 0.8 kcal/mol, which is ∼8 kcal/mol more favorable to be delivered into a cell membrane than bexarotene (insertion free energy = 12.2 ± 0.9 kcal/mol).

***In Vitro* Experiments.** HepG2 cells were treated with bexarotene, pro-bexarotene, PBNB, and NB formulations to establish their cytotoxicity in the absence of US. $IC_{50}$ values for bexarotene, pro-bexarotene, and PBNB formulations were ∼25, 60, and 45 $\mu$M, respectively. At 100 $\mu$M, the trend of hepatocellular carcinoma cell (HCC) growth response remained the same with maximum cell death observed in the case of bexarotene (∼95%) followed by PBNB (∼70%) and pro-bexarotene (∼60%). A two-way ANOVA analysis was performed to determine the statistical signficance of the results. Cell viability studies showed a statistically

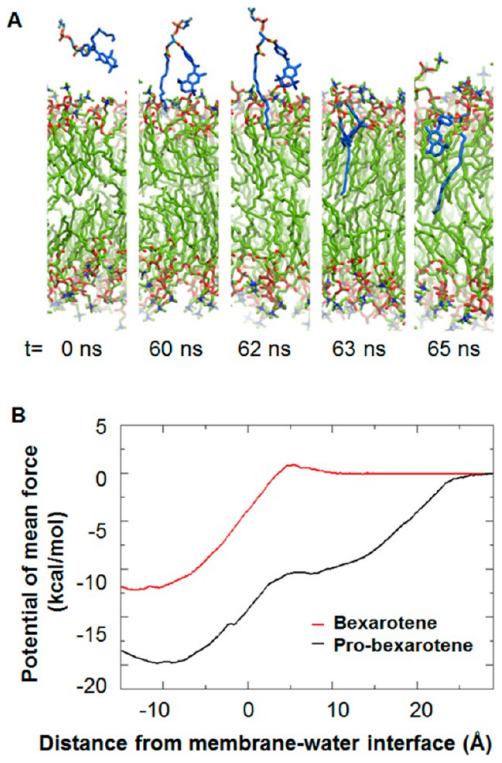


**Figure 5. Static snaps of molecular dynamics simulations of the insertion process of pro-bexarotene into a membrane after US exposure to PBNBs (top). The bexarotene group in the prodrug inserts more favorably into the membrane than does bexarotene by itself (bottom).**

significant decrease in the case of bexarotene treatment at concentrations of 30, 60, and 100 $\mu$M (Figure 6A). Similar results were obtained for treatments at 48 and 96 h, while PBNB improved its efficiency with increased incubation time, and bexarotene allowed more cells to revive their viability at the time point of 96 h (Figure S3). Upon optimization of the US parameters using a sub-$IC_{50}$ concentration of 5 $\mu$M, for PBNB formulation, a significant drop in % cell viability was reported ($p < 0.05$; one-way ANNOVA with Bonferroni post-test) compared to non-US-exposed cell population (Figure 6B). These effects could be visualized under bright-field microscopy for US-exposed or unexposed cell populations (Figure S4).

Experiments were further performed to optimize the concentration of PBNB at optimized US exposure for better growth regression. MTT results show the improvement in $IC_{50}$ values of PBNBs to ~13 $\mu$M (Figure 6C). Biostatistical analysis (two-way ANOVA with Bonferroni post-test) of MTT results showed improved cell growth regression at a time point of 72 h with a treatment concentration of 15 $\mu$M (Figure 6C). It was revealed the improvement of the cell regression ability of PBNB on US exposure by a significance of $p < 0.005$ at concentrations of 15, 7.5, 3.75, and 1.87 $\mu$M compared to NB treatment at the same concentration. Further statistical analysis by comparison of PBNB and NB treatments in the absence and presence of US revealed the decrease in cell viability with PBNB compared to that of NB by $p < 0.5$, while under US exposure, it improved by a significance of $p < 0.05$. NB on the other hand did not reduce the % cell viability to any significant level (Figure 6D). It is anticipated that the major role of US exposure is to facilitate the rupture of the prodrug bubble and assist the internalization of PBNB and NB at the surface of HCC. The US has no role to delegate the functional activity of bexarotene after delivery. Further MTT assay performed on HCC cells for 120 h at concentrations of 50, 25, 12.5, 6.25, and 3.125 $\mu$M revealed reduced cell viability only at a higher concentration of 25 and 50 $\mu$M (Figure 6E) compared to 72 h treatment with 15, 7.5, 3.75, and 1.87 $\mu$M (Figure 6C). Lower concentration of 12.5, 6.25, and 3.125 $\mu$M did not show any improvement in cell growth regression with an extended incubation period post-US exposure. These analyses verify the combinatorial effects of HCC growth regression of PBNBs and US exposure. Cellular assay results were also corroborated with bright-field microscopy images (Figures S5 and S6). PBNBs were found to be highly effective in deteriorating the growth density and morphology of HCC cells at 15 $\mu$M concentration (Figure S5H). In Figure 6C,D, the cell viability without US was ~100% for NB (no bexarotene), whereas with PBNB, Figure 6D shows a decrease in cell viability to ~65% at 10 $\mu$M, and US exposure further reduced it to ~45%. Hence, NB exhibited no significant damage to HCC even in the presence of lipases.

**Mechanistic Studies of RXR Modulation and Probing Other Biological Interactions for PBNB and Controls.** Mechanistic studies on the role of US-facilitated PBNB treatment in induction of apoptosis were performed *in vitro* using analysis on sub-$G_0/G_1$ cell population in a cell cycle study and genomic DNA fragmentation assay. The fate of apoptotic death leads to cell shrinkage, membrane blebbing, and fragmentation of genomic DNA into oligonucleosomal subunits. Staining of cells after apoptosis with propidium iodide (PI) allows very low PI intercalation in fragmented genomic DNA, leading to a low-fluorescence cell population in the cell cycle analysis. Thus, the apoptotic cell population can be categorized as the lowest PI staining population during the cell cycle analysis, which can also be identified as the sub-$G_0/G_1$ cell population. A PI staining assay was performed on HepG2 cells ($1.5 \times 10^5$ plated in a 12-well plate) after treatment with PBNB for 72 h post-US exposure. The % apoptotic cell population was quantified (Figure 7A−C) as ~95 and 74% cells for treatments with PBNB+US at concentrations of 50 and 12.5 $\mu$M (Figure 7B,C), represented as the red population compared to cells with no significant apoptosis in the case of untreated cells (Figure 7A).

Cellular apoptosis ultimately causes the nuclear fragmentation into small, condensed, membrane-bound apoptotic bodies. The genomic DNA results into

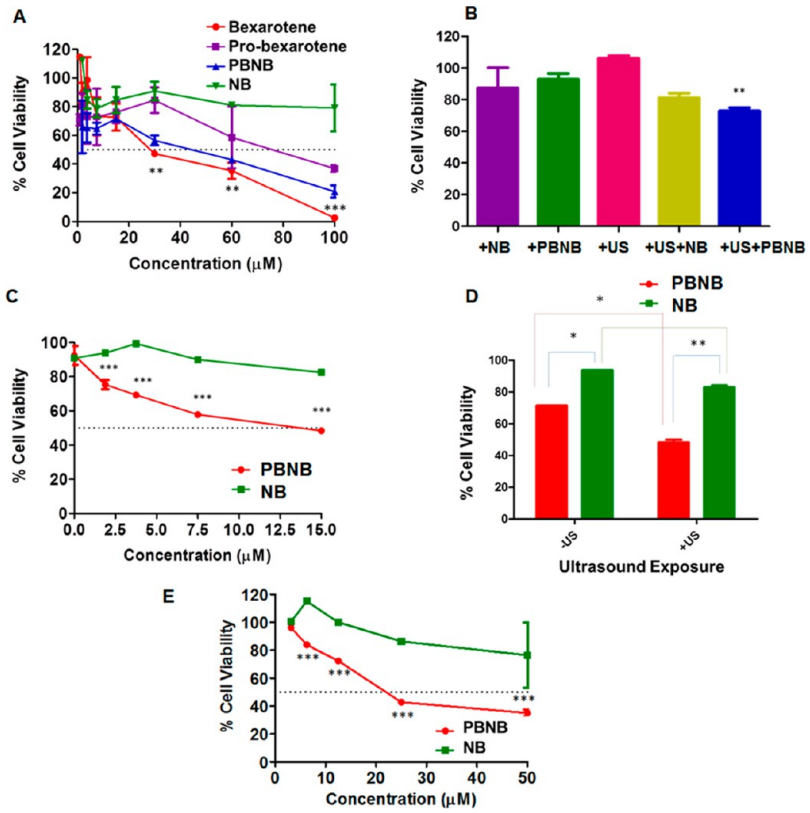


**Figure 6.** *In vitro* **MTT assay experiments for establishing HCC growth regression in HepG2 cells after 72 h of incubation. (A) MTT assay on HepG2 cells treated with formulations to establish effective concentrations after 72 h of treatment. (B) Optimization of US parameters for establishing effective improvements in US-mediated enhancements in growth regression of HepG2 cells after 24 h treatment with 5 $\mu$M. (C) Effect of therapeutic nanobubble, PBNB, on HCC growth regression after optimized US exposure at a time point of 72 h at concentrations of 15, 7.5, 3.75, 1.87, and 0.93 $\mu$M. A two-way ANOVA was performed and showed a biologically significant difference in cell growth inhibition efficiency between PBNB and NB at all used concentrations. (D) Biostatistical significance of therapeutic nanobubble (PBNB) treatment and US exposure at a concentration of 10 $\mu$M for 72 h in HepG2 cells. (E) Effect of therapeutic nanobubble, PBNB, on HCC growth regression after optimized US exposure at a time point of 120 h at concentrations of 50, 25, 12.5, 6.25, and 3.125 $\mu$M.**

nucleosome-sized pieces of approximately 200 bp and multiples thereof, generating 3′-OH groups at the strand breaks. A gel laddering experiment performed on extracted genomic DNA from treated cells revealed the efficiency of inducing cellular apoptosis in HepG2 cells after treatment with PBNB and other control formulations. It was found that the electrophoretic mobility of genomic DNA from cells treated with 12.5, 25, and 50 $\mu$M PBNB (Figure 7D, lanes 4, 5, and 6) could show a ladder of increasing intensity, while no significant response in NB-treated cells at 25 and 50 $\mu$M (Figure 7D, lanes 7 and 8) was noticed. Induction of DNA fragmentation further confirmed the role of PBNB for induced apoptosis in HepG2 cells.

**Interaction of Bexarotene with Duplex Plasmid DNA and Effect of Its Prodrug and Nanobubble Form on Electrophoretic Mobility.** Interaction of pDNA with bexarotene (Figure 7E, lanes 1−3), PBNB (Figure 7E, lanes 8−11), and NB (Figure 7E, lanes 12−14) resulted in no change in the gel retardation pattern of pDNA. Change in gel retardation was noticed when the concentration reached 1−10 molar ratio with pDNA (Figure 7E). A 1:5 molar ratio (lane 5) was enough to exhibit considerable interaction and gel retardation for pro-bexarotene, showing approximately 20% pDNA binding to pro-bexarotene (Figure 7E). To further clarify the role of nanobubble assembly in loosening the pDNA interaction of pro-bexarotene, PBNB−pDNA mixtures were compared with mixtures of pro-bexarotene DNA at 10−25 molar ratios (Figure 7F). An incremental binding pattern was clearly visualized for pro-bexarotene (lanes 15−18), while a PBNB−pDNA mixture was found to be noninteracting at all ratios (lanes 21−24). Further increase in molar ratios resulted in distinguishable changes in the pDNA interaction pattern of pro-bexarotene (Figure 7G, lane 26) compared to PBNB (Figure 7G, lane 25). Overall evaluation of pDNA interaction studies led to the conclusion that pro-bexarotene transformed into a stable nanoassembly (PBNB). It also showed the inability of PBNB and its chemical components to generate DNA fragments *via* DNA cleaving. This further signifies the induction of apoptosis in DNA fragmentation processes.

**RXR Agonist Assay.** RXRα activity of bexarotene in free (bexarotene), pro-drug (pro-bexarotene), and pro-drug

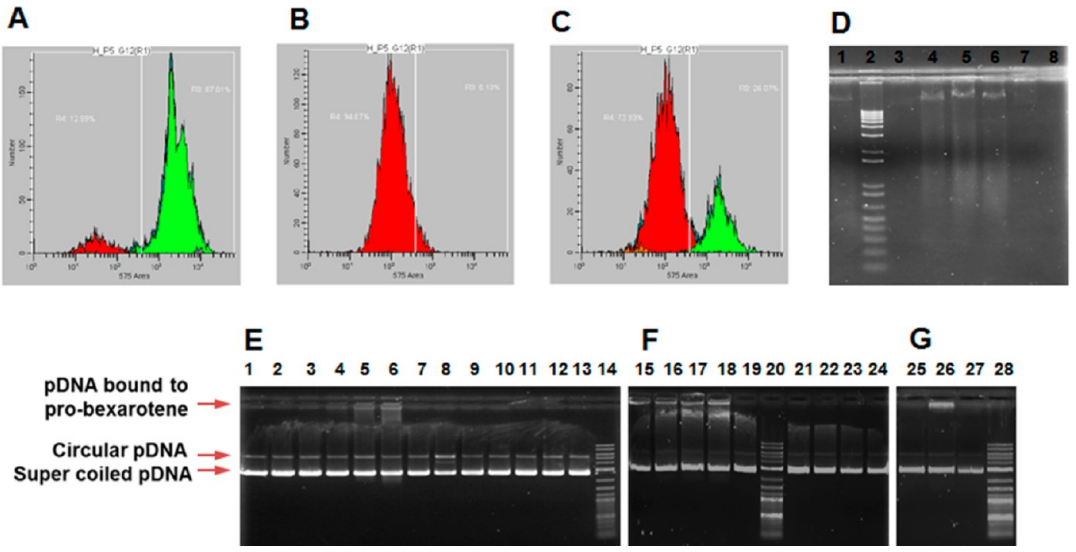


**Figure 7. Mechanistic studies on role of US-facilitated PBNB treatment in the induction of apoptosis and interaction of bexarotene with duplex plasmid DNA (pDNA). Experiments were performed on HepG2 cells ($1.5 \times 10^5$ plated in a 12-well plate), post-treated with PBNB for 72 h after US exposure. PI staining on the fixed cell population after US treatment only (A), and treatments with PBNB+US at concentrations of (B) 50 and (C) 12.5 $\mu$M showed around 95 and 74% cells going through apoptosis (red populations), respectively. (D) Gel laddering experiment performed on extracted genomic DNA from treated cells. It represents electrophoretic mobility of genomic DNA from cells treated with PBNB: lane 1, untreated; lane 2, 1 kb ladder; lane 3, 6.25 $\mu$M; lane 4, 12.5 $\mu$M; lane 5, 25 $\mu$M; lane 6, 50 $\mu$M and treated with NB; lane 7, 25 $\mu$M; lane 8, 50 $\mu$M. Cells treated with 12.5, 25, and 50 $\mu$M of PBNB-produced DNA ladders, implying that the cells have gone through apoptosis. (E−G) Interaction of bexarotene with duplex plasmid DNA (pDNA) and the effect of its prodrug and nanobubble form on electrophoretic mobility. Experiment was performed using (E) 500, (F) 250, and (G) 250 ng of pBR322. (E) pDNA was incubated at the following molar ratios: (with bexarotene) lane 1, 1:1; lane 2, 1:5; lane 3, 1:10; (with pro-bexarotene) lane 4, 1:1; lane 5, 1:5; lane 6, 1:10; (with PBNB) lane 8, 1:1; lane 9, 1:5; lane 10, 1:10; and (with NB) lane 11, 1:1; lane 12, 1:5; lane 13, 1:10; lane 7, DNA alone; lane 14, 0.1−1 kb DNA ladder. (F) pDNA was incubated: (with pro-bexarotene) lane 15, 1:10; lane 16, 1:15; lane 17, 1:20; lane 18, 1:25; (with PBNB) lane 21, 1:10; lane 22, 1:15; lane 23, 1:20; lane 24, 1:25; lane 19, DNA alone; lane 20, 0.1−1 kb DNA ladder. (G) pDNA was incubated: (with pro-bexarotene) lane 26, 1:30; (with bexarotene) lane 27, 1:30; lane 25, DNA alone; lane 28, 0.1−1 kb DNA ladder.**

nanobubble (PBNB) form was measured at concentrations of 0.5, 5, and 50 $\mu$M. A positive control of 9-*cis*-retinoic acid was used as a positive control at a concentration of 5 $\mu$M. Luminescence was measured at various time points, including 5 min (Figure 8A), 10 min (Figure 8B), 15 min (Figure 8C), 20 min (Figure 8D), 25 min (Figure 8E), 30 min (Figure 8F), 35 min (Figure 8G), 40 min (Figure 8H), 45 min (Figure 8I), and 50 min (Figure 8J). Changes in luciferase activity was proportional to RXRα activity post-treatments. Invariably, PBNB was found to be a better RXRα agonist compared to bexarotene and pro-bexarotene molecules at a concentration of 0.5 $\mu$M. At a concentration of 5 $\mu$M, bexarotene was better than PBNB and pro-bexarotene on the same order, while response at 50 $\mu$M was very similar to no significant difference among any of the used formulations. Change in luciferase activity was summarized to see maximum RXRα agonist efficiency in the case of PBNB at 0.5 $\mu$M followed by pro-bexarotene and bexarotene at various incubation time points (Figure 8K). Luciferase assay revealed the improvement in RXR activity on conversion of free bexarotene to pro-bexarotene and further to PBNB to improved cell internalization. This was also predicted by molecular dynamics simulations and density functional theory distribution studies.

***Ex Vivo* Experiments.** *Ex vivo* experiments were conducted using a freshly excised porcine liver tissue sample. The tissue sample was placed in a thermoelectric enclosure to maintain the tissue temperature at 35−37 °C during the experiment (Figure 9). TheraVision (Acoustic MedSystem, IL) ultrasound ablation system and Acoustx applicators[47] were used to deliver high-intensity ultrasound energy to the target tissue volume (Figure 9A−D). The PBNB was injected into the tissue using a 21 gauge needle under ultrasound image guidance (Figure 9E,F). The strong acoustic reflection from the needle could be easily identified in the ultrasound B-mode image, including the release of the nano-chemotherapeutics at the tip of the needle shown in Figure 9F. Needle thermocouples of type T (Physitemp, New Jersey, USA) with multiple sensors along the needle length were used for monitoring temperature during the treatment. Each needle was $100 \pm 2$ mm long and 0.82 mm in diameter with 0.1 °C accuracy. Thermocouples were placed at different distances from the ultrasound applicator, and dose was calculated for each thermal sensor (Figure 9G−I).

The template helped to precisely register the location of each thermocouple with respect to the ultrasound applicator. Acoustic power of 6 W per element was delivered to the tissue for the initial 2 min and then

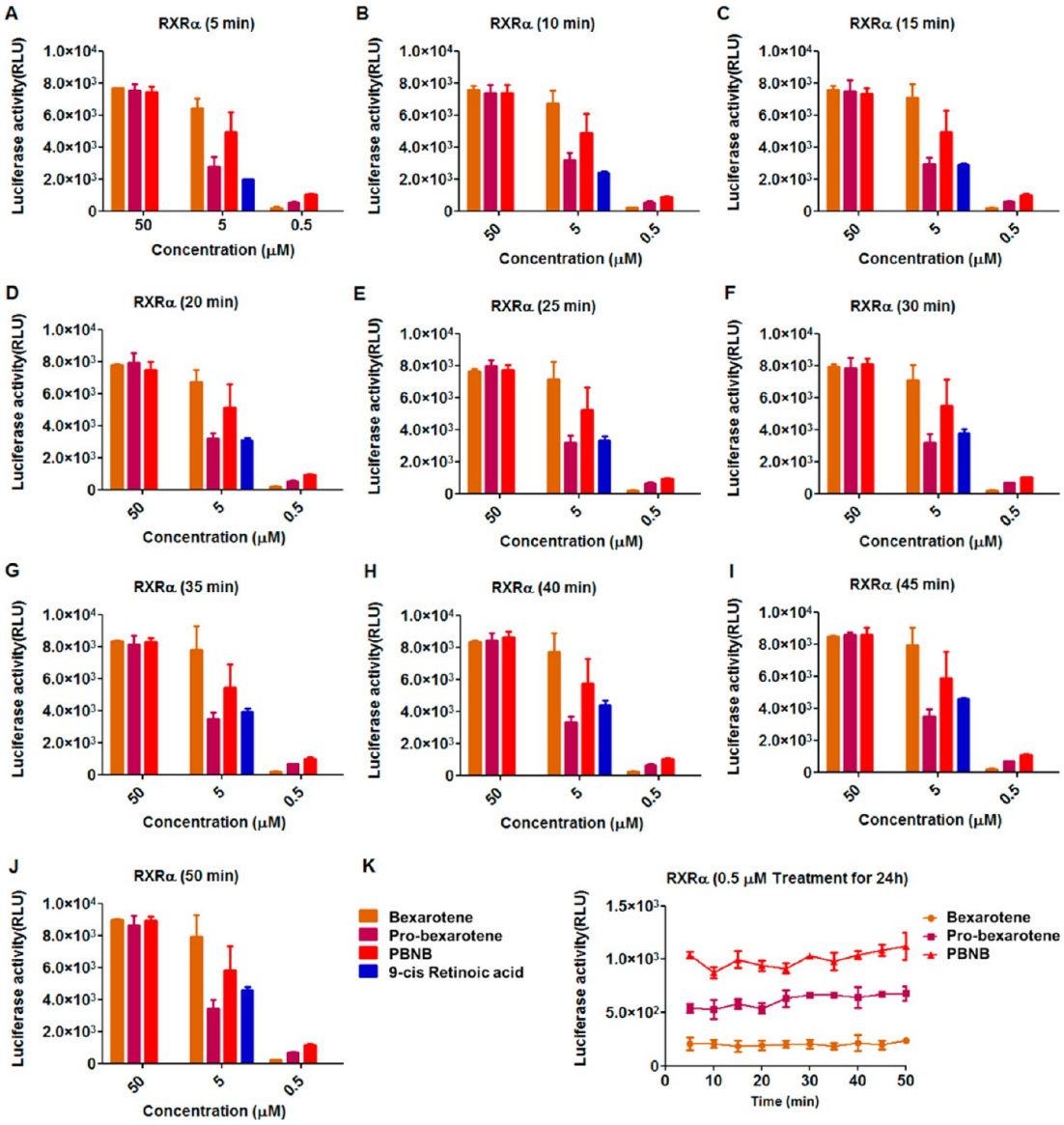


**Figure 8. RXRα activity of retinoid bexarotene in free (bexarotene), pro-drug (pro-bexarotene), and pro-drug bubble (PBNB) form at concentrations of 0.5, 5, and 50 μM. A positive control 9-*cis*-retinoic acid was used at the positive control at a concentration of 5 μM. After addition of luciferase substrate, luminescence was measured at various time points including (A) 5 min, (B) 10 min, (C) 15 min, (D) 20 min, (E) 25 min, (F) 30 min, (G) 35 min, (H) 40 min, (L) 45 min, and (J) 50 min. (K) Change in luciferase activity with time was summarized only to see maximum RXRα agonist efficiency in the case of PBNB at 0.5 followed by pro-bexarotene and bexarotene.**

increased to 7 W with a total treatment time of 6 min for each experiment. The gross pathology images (Figure 10A−D) show red spots, indicated by the white arrows in Figure 10A,B,D, to indicate the diffusion of the rhodamine into the tissue post-US ablations. The temperature profiles at various locations are shown in Figure S8. The thermocouple sensor TC-B placed between the two applicators shown in Figure S9 shows the highest rise in temperature due to the combined ablation effects contributed from both of the applicators. The TC-C placed at 10 mm radially beside applicator 2 shows a large rise in temperature during the ablation. TC-A exhibited a less rapid increase as it was located the greatest distance from both US treatment applicators. Typically, necrosis occurs above 43 °C and is time-dependent. Temperature rise above 43 °C was observed in all cases at 15 mm radially from the applicator. The gross pathology images shown in Figure 10A−F show a good ablation pattern created using the dual applicator configurations. Approximately, a similar lesion size was observed in all cases. Temperature sensors were inserted into the tissue to monitor temperature profiles and accumulated thermal dose to determine the thermal necrosis zones and also define the safety margin and its reproducibility. Temperature rise of different extents can produce different resultant tissue damage levels, including reversible and irreversible damage. The measured temperatures

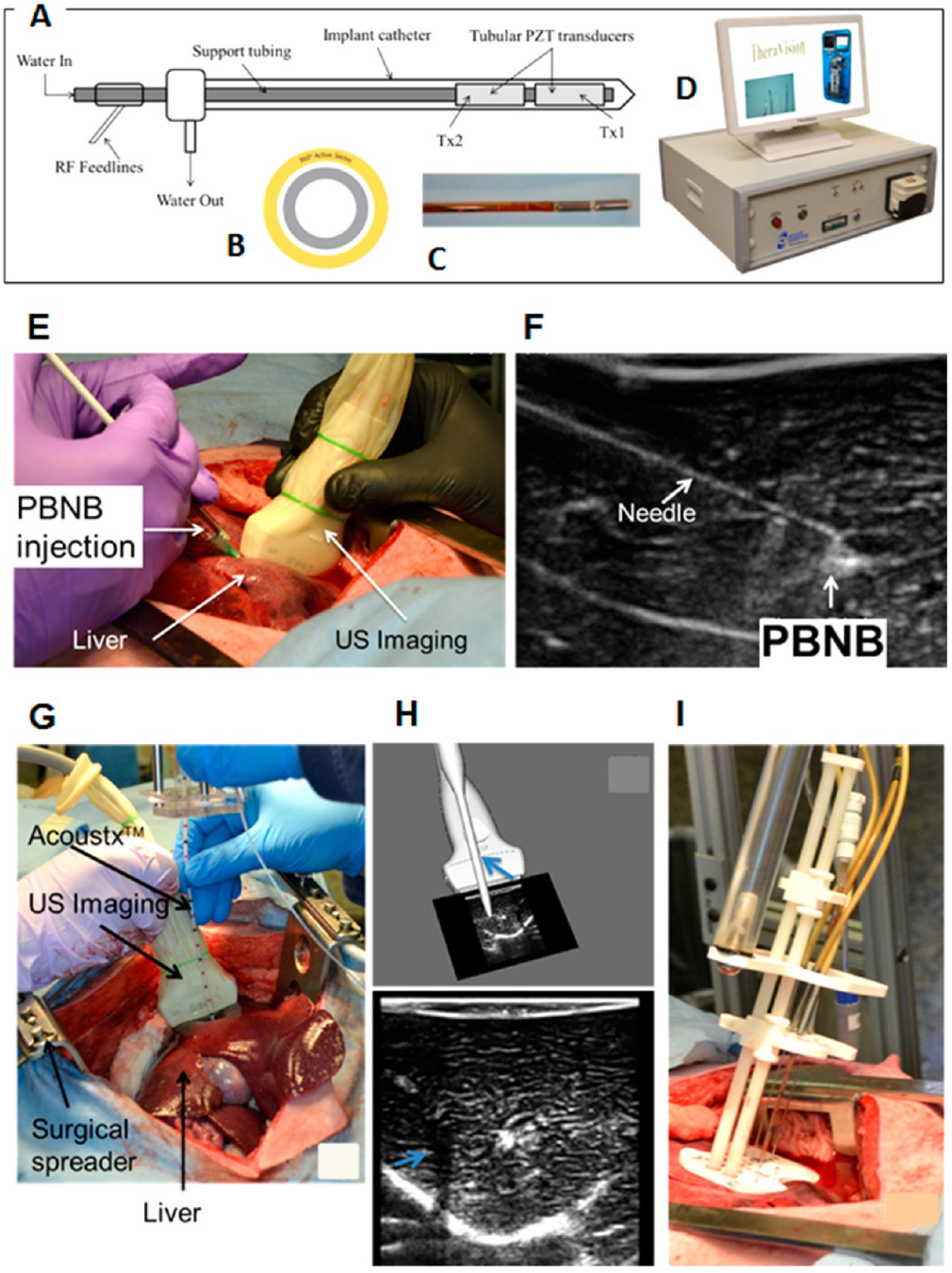


**Figure 9. (A) Schematic of a catheter-based ultrasound (CBUS) applicators for percutaneous conformal hyperthermia and thermal ablation to targets in soft tissue. (B) Sectored tubular ultrasound transducer showing 360° sector design for creating an ablation pattern during the treatment. (C) Magnified view of fabricated interstitial CBUS applicator tip showing the two transducers. Each of these transducers can be controlled individually with respect to the needed dose delivery. (D) Table-top TheraVision ablation system, which includes image processing and therapy control algorithms. (E) Injection of PBNB under 3D tracked ultrasound image guidance and (F) corresponding ultrasound B-mode showing the needle insertion and PBNB injection site. (G) Insertion of ultrasound Acoustx applicators under the guidance of combined ultrasound imaging and electromagnetic tracking. (H) Ultrasound imaging and applicator position in the 2D and 3D planes corresponding to the setup shown in (H) (arrows indicate the catheter in the 3D view and shadow by the catheter in the B-mode image). (I) Template with applicator and fine needle thermocouples during treatment.**

and the accumulated resultant thermal dose estimated from inserted fine needle thermocouple arrays aided in determining the damage level due to the treatment. In other studies, a temperature rise of more than 35 °C was observed during focused ultrasound ablation of uterine fibroids.[50] Similar temperature rise of more than 30 °C above body temperature was observed in RF ablation of a liver tumor in a 71 year old patient.[51] In both of these cases, researchers used a magnetic resonance temperature imaging (MRTI) method to monitor

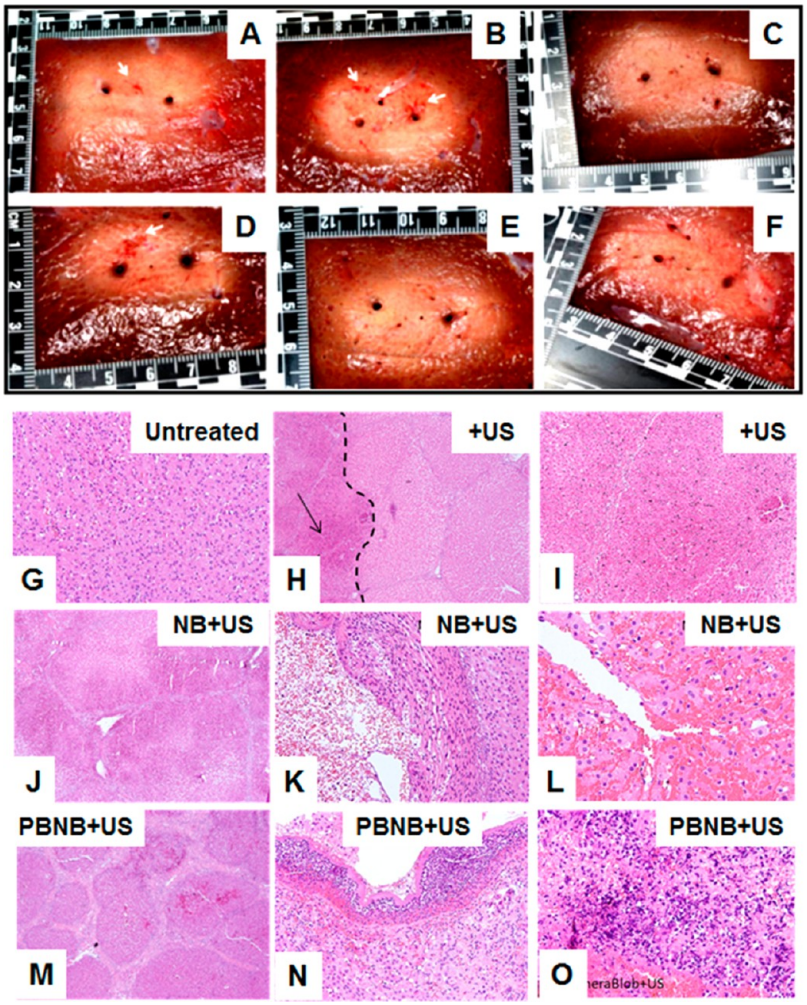


**Figure 10. (A) Gross pathology images for the different configurations from *ex vivo* experiments: (A) Pro-bexarotene NPs (RD) + US, (B) NB (RD) + US, (C) Pro-bexarotene NPs (RD) + US ablation, (D) PBNB (RD) + US ablation, (E) PBNB + US ablation, (F) US ablation only. The white arrows in (A−D) indicate the presence of rhodamine (RD) around the site of injection. Histopathology images obtained from liver tissues from *in vivo* experiment of (G) normal liver at 8× magnification, (H) liver ablated with ultrasound at 2× (the dotted line indicates the boundary of the ablated and normal tissue (right), and the arrow points to the ablated region (left)). (I) Magnified ultrasound-treated region marked by arrow in (J) at 8× US only indicates prenecrotic hepatic damage. (K) Liver tissue treated with ultrasound in the presence of nanobubbles, showing signs of injury and sinusoidal dilation edema of hepatocytes at 4×, with 50% of region showing frank necrosis. (L) Necrotic region, thermal damage, and streaming in ∼50% of area shown at 20× and (M) areas of hemorrhage and bubble in cytoplasm (70%) at 40×. Liver tissue treated with combined therapy of high-intensity ultrasound and PBNB showing (J) liver bands due to contraction of liver parenchyma in the vicinity of the necrotic area at 4×. (K) Liver capsule, inflammation, and acute signs of frank necrosis in the liver over the entire area shown at 20×. (L) Total (100%) necrotic area of dead tissue, with inflammation at 40×. (M) PBNB-injected liver tissue, (N) PBNB-injected normal liver with stress and slight hemorrhage at the injection site, and (O) PBNB injected normal liver with hepatoportal tract and no pathological change.**

the temperature profile during ablation of the respective tissues. In another study, researchers used MR-guided RF ablation of liver tumors and observed an increase of temperature ranging from 60 to 100 °C, very near the treatment device in the tumor region during ablation.[52] In microwave treatment of porcine renal cortex experiments, a temperature rise of more than 85 °C at the tip of the antenna was observed.[53] In this study, similar temperature rises ranging from 15 °C at 15 mm to ∼40 °C at 5 mm were observed in *in vivo* porcine liver, during ablation with Acoustx applicators in the presence of PBNB. Tissue temperature of 70−76 °C was observed at 5 mm radial distance from the axis of the applicators.

***In Vivo* Experiments in a Swine Model for Optimization of the Therapy Regime.** *In vivo* experiments were conducted in porcine liver. A custom template was used to insert the applicator and thermocouples, as shown in Figure 9. Real-time 3D tracked ultrasound image guidance was used to insert the Acoustx applicator (Figure 9A,B). The targeted liver was exposed to high-intensity ultrasound delivered *via* Acoustx applicators for 8 min at an acoustic power level of 7 W. From gross tissue images, the lesion diameter of 2.4 ± 0.1 cm and axial length of 2.0 ± 0.1 cm were observed repeatedly for high-intensity ultrasound exposure using consistent energy delivery parameters. The temperature and

**TABLE 3. Mean Peak Temperature and Accumulated Thermal Dose at Various Radial Distances from the Applicator for a Single Applicator Insertion Configuration**

| | peak thermometry at different radial distances | | | | | | | |
|---|---|---|---|---|---|---|---|---|
| | 5 mm | | 10 mm | | 15 mm | | 20 mm | |
| tissue | $T$ (°C) | $t_{43}$ (min) | $T$ (°C) | $t_{43}$ (min) | $T$ (°C) | $t_{43}$ (min) | $T$ (°C) | $t_{43}$ (min) |
| liver | 73.9 ± 2.9 | $5.64 \times 10^8$ | 63.8 ± 3.2 | $1.65 \times 10^6$ | 47.2 ± 0.6 | 154.3 | 44.7 ± 1.1 | 6.1 |

accumulated thermal dose at various radial distances from the therapy applicator are tabulated in Table 3. The radial distance at a thermal dose of $t_{43} > 240$ min was estimated as $R = 15$ mm, by interpolating the data shown in Table 3. This distance $R$ defines the thermal necrosis boundary and margin of the treatment. Specifically, $R$ was estimated by interpolating thermometry data at various radial distances and angles from the axis of the applicator. Highest temperatures were recorded at the 5 mm radial distance. Temperature of the applicator catheter did not exceed 36 °C. Temperatures sufficient to produce a thermal dose of at least 240 equivalent minutes were measured for nearly all cases at a radial distance of 15 mm from the applicator center (30 mm diameter treatment zone). Since liver is a highly vascularized organ, the drug injected into the target site will also circulate to other organs, and hence the prodrug formulation can be delivered through either a direct or a vascular route. The vascular delivery approach was out of scope for this work; however, it may be conducted as a separate study in the near future. The thermal damage end points can be classified into vascular effects, direct damage, and functional effects. Histopathological analysis is considered to be the gold standard to understand the tissue effects and damage due to various types of therapy, including thermal energy therapy. Cancer cells are durable and resistive enough to insult that they can recover from a harsh environment if not completely destroyed. Histopathological analysis can be used to confirm tissue damage at the cellular level due to thermal therapy. Histopathological and gross appearance of tissue damage was observed at a thermal dose greater than $t_{43} > 240$ min in various studies of *in vivo* tissue including liver, muscle, prostate, and kidney from dog, rabbit, and pigs, as reported by numerous studies.[48]

Histopathology images were analyzed to detect tissue damage resulting from the combined therapy (high-intensity ultrasound plus PBNB). Tissues from four different experimental configurations, (i) untreated, (ii) US only, (iii) US and nanobubble, and (iv) US and PBNB, are shown in Figure 10G−O. Specifically, liver tissue was analyzed for histological features. Both normal and thermally damaged tissue was analyzed to differentiate histological changes between them. Histopathology of normal liver shows healthy cell distribution (Figure 10G), while hepatocyte balloon degeneration, liver "congestion", and minor sinusoidal dilation are evident for high-intensity ultrasound treatment (Figure 10H,I). The tissue treated with high-intensity ultrasound in the presence of nanobubbles exhibits area of necrosis, thermal coagulation, sinusoidal dilation edema of hepatocytes, streaming, hemorrhage, and bubbles in the cytoplasm (Figure 10J−L). Liver tissue treated with the combined treatment of PBNB and high-intensity ultrasound showed bands due to contraction of liver parenchyma in the necrotic region, inflammation sign of stress, dead tissue, and thermal coagulation (Figure 10M−O). Cell bursting was also observed. Liver tissue treated with ultrasound in the presence of nanobubbles (no drug) indicates signs of injury and sinusoidal dilation edema of hepatocytes at 4×, with 50% of the region showing frank necrosis and necrotic region, thermal damage, and streaming in ∼50% was seen at 20×. At 40×, the area of hemorrhage, the bubble in the cytoplasm (70%), was seen. Liver tissue treated with combined therapy of high-intensity ultrasound and PBNB shows liver bands due to contraction of liver parenchyma in the vicinity of the necrotic area at 4× and liver capsule, inflammation, and acute signs of frank necrosis in the liver over the entire area at 20×. Total (100%) necrotic area of dead tissue with inflammation was noticed at 40×. PBNB-injected normal liver tissue shows signs of stress and slight hemorrhage at the injection site along with the hepatoportal tract having no pathological change.

***In Vivo* Study in Transgenic Tumor-Bearing Swine Model.** A liver cancer animal model that can be used for studying this trimodal ablation therapy was not immediately available. Furthermore, the use of a flexible ablation catheter, developed for human use in mind, precluded us from using a rodent-based tumor model. The comparable size of the pig and its resemblance in anatomy, physiology, metabolism, and genetics to humans make it an attractive platform to develop a genetically defined, large animal model of cancer. To this end, in a preliminary experiment, we tested the combination of PBNB and US ablation in a transgenic "oncopig" line encoding Cre recombinase inducible porcine transgenes encoding KRASG12D and TP53R167H.[49] These genes are known to represent a commonly mutated oncogene and tumor suppressor in human cancers. Due to the study limitation and unavailability of a tumor model grown in swine liver, an improvised

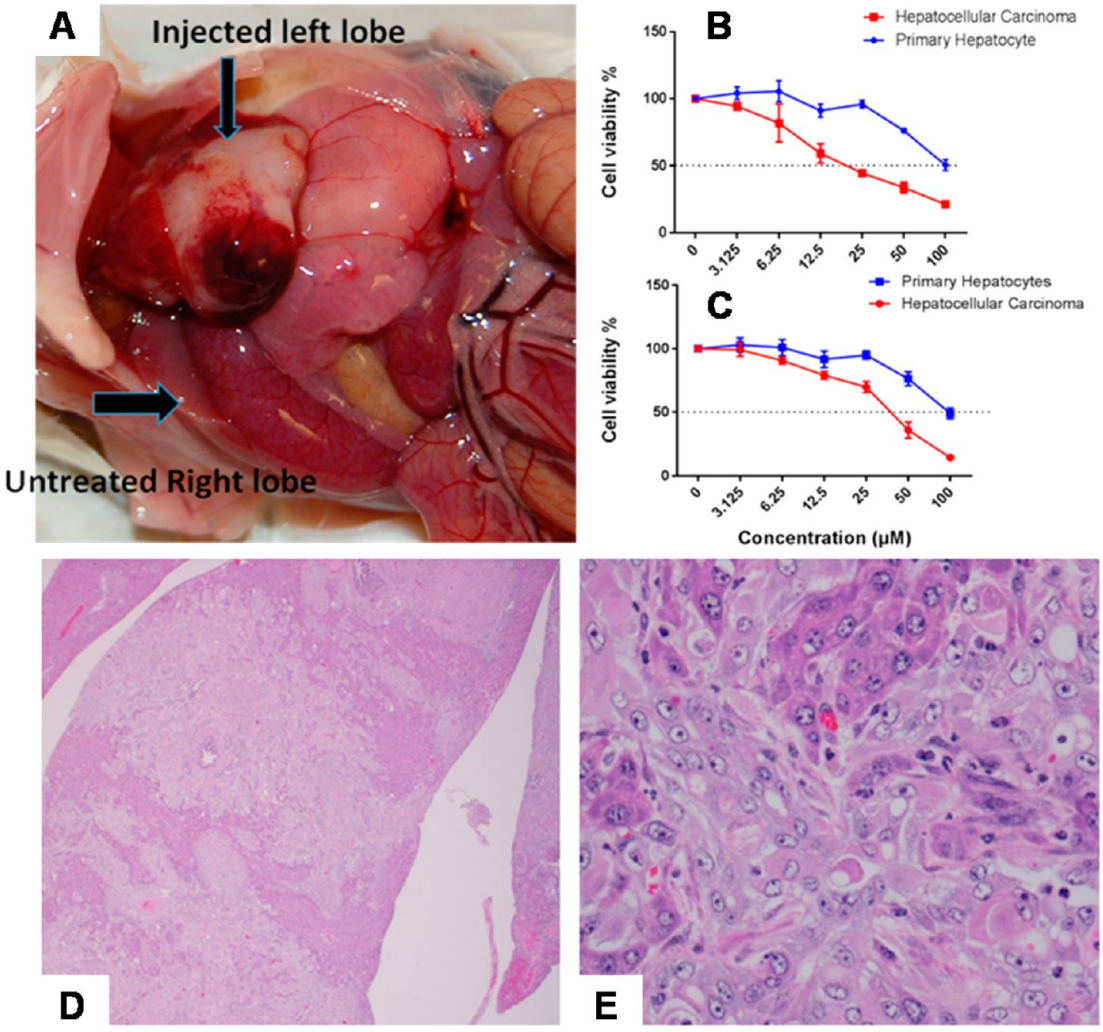


**Figure 11. (A) Left lobe of mouse liver injected with transformed hepatocytes, indicating the development of a tumor, whereas the untreated right lobe appeared normal. *In vitro* assessment of drug activity as a free small molecule bexarotene (B) or PBNB (C) by using MTT assay at 72 h. H&E stained sections of mouse liver transplanted with transformed hepatocytes. (D) Dissecting through the liver shows sheets of transplanted cells. Bile ducts exhibit hyperplasia (1.2×). (E) Transplanted cells arranged in sheets and trabeculae and supported by a thick fibrous stroma. Individual transplanted round to polygonal cells with moderate quantities of light eosinophilic homogeneous cytoplasm and surrounded by an indistinct cell border. Nuclei appeared single to multiple, round to oval, with scattered chromatin and a single prominent central nucleolus. Small numbers of neutrophils look scattered within these regions. Existing trapped hepatocytes exhibit atrophy (3.40×).**

approach was taken. Based on this approach, the liver hepatocyte cells were removed from the oncopig, implanted into the mouse liver, and the tumors regrown. The transformed liver tumor cells were used to assess the therapeutic efficacy of PBNB. Liver tissues obtained from the mouse were histologically analyzed for characteristics of HCC.

Briefly, hepatocytes were isolated from transgenic oncopig, containing mutated oncogene Kras ($Kras^{G12D}$) and p53 ($p53^{R167H}$) in their genome. $Kras^{G12D}$ and $p53^{R167H}$ mutants were linked by internal ribosome entry sites (IRES) for their simultaneous expression. The cassette was then inserted into a vector following the LoxP−PolyA (STOP)−LoxP sequence. Hepatocytes were isolated from this transgenic oncopig and transfected with Cre plasmid, which delegates the PolyA "STOP" sequence and allows transgene expression.[49] Histopathology of these cells revealed that they were of HCC nature. The transformed hepatocyte cells were able to successfully generate hepatocellular carcinoma in mouse liver (Figure 11A−E). As shown in Figure 11A, the injected left lobe of the mouse liver with transformed hepatocytes developed tumor, whereas the untreated right lobe appeared normal. The histopathological analysis on liver tissues excised from mouse liver injected with transformed hepatocellular carcinoma revealed the presence of numerous transplanted cells (Figure 11D,E) These cells were arranged in trabeculae and rare acini supported by a thick fibrovascular stroma. Individual transplanted cells were round to polygonal with a moderate amount of light eosinophilic cytoplasm surrounded by an indistinct cell border. Nuclei were single to multiple, round to oval, with scattered chromatin and a single prominent nucleolus.

These cells exhibited moderate anisocytosis and anisokaryosis. Mitotic figures were 2 per 10 high power fields. Areas of necrosis and hemorrhages were found to be scattered within these regions. The adjacent hepatocytes exhibited atrophy. Small numbers of neutrophils were also scattered within these regions. Thus, the injected liver was found to have multiple islands of proliferating viable transplanted cells. These features confirm the morphology of these cells resembling transplanted transformed hepatocytes and the possible nature of a hepatocellular carcinoma. It was found that they were able to produce a tumor in the mouse liver. The transformed hepatocytes were used for further *in vitro* assessment of drug activity as either a free small molecule or PBNB. Results indicated a significant cellular regression and improvement in $IC_{50}$ value of bexarotene in the form of prodrug-derived PBNB (Figure 11B,C). Altogether, the results indicated that even though it was not possible to generate a direct tumor implanted in swine liver, we achieved therapeutic efficacy in a tumor equivalent *in vivo* model.

**Tumor Destruction and Histopathological Analyses Post-US Exposure.** Under an approved protocol by the University of Illinois Institutional Animal Care and Use Committees (IACUC), transgenic oncopig was grown as described before.[49] As a makeshift strategy for the assessment of tumor regression *in vivo* with thermal ablation combined with drug treatment, 5 week old transgenic piglets were infected with virus at specific sites of right and left thigh. Animal was kept under observation until the tumor grew to significant size (1.5 cm $\times$ 1.5 cm). Tumor growth was followed by US imaging using a hand-held US imaging machine (Figure 11). Figure 12 indicates the formation of abnormal tissue growth in the (A) right and (B) left thigh of a representative transgenic pig. Abnormal tissue growth was regularly followed until treatment with PBNB (1 mg/mL, 5 mL total volume) and US.

Tumor destruction was followed by histopathological analyses after animal necropsy (Figure 12C−E). Figure 12F,G shows the presence of neoplastic cells, which are spindeloid to round and contain a round nucleus and light eosinophilic cytoplasm surrounded by an indistinct cell border. Nuclei are single, round with scattered chromatin and multiple prominent nucleoli. Neoplastic cells stained strongly with anti-CD31 antibody confirm the presence of endothelial cells. Therefore, it can be concluded that the tumors are of angiosarcoma type. Scattered within the neoplastic cells are small numbers of lymphocytes and plasma cells. Figure 12H shows the skeletal muscle bundles not treated with thermal ablation. Absence of US treatment is evident here. Figure 12I shows the skeletal muscle fibers treated with thermal ablation, exhibiting sarcoplasmic hyalinization, loss of striation, cell shrinkage, and increased endomysial space. Figure 12J also confirms the presence of skeletal muscle fibers treated with thermal ablation, exhibiting sarcoplasmic hyalinization, loss of striation, cell shrinkage, sarcoplasmic fragmentation, and increased endomysial space. Lymphocytes and plasma cells are infiltrating endomysial regions. Figure 12K shows the presence of neoplastic cells in the tumor from the right thigh, exhibiting mild cytoplasmic swelling and vacuolation. This observation indicates vacuolar degeneration. The abundance of vacuolar degeneration is indicative of the drug treatment.

A detailed necropsy investigation was performed on the treated pig. As evident from our studies, the presence of multifocal areas of atelectasis and hemorrhage within the airways and alveolar spaces in the lung was noticed. There are rare subcapsular areas of acute hemorrhages observed in liver. Hepatocytes in some regions are mildly swollen and contain granular cytoplasm with a central nucleus. Multiple secondary lymphoid follicles are present in the spleen. No significant lesion was observed in the gall bladder, thyroid gland, lymph nodes, thymus, adrenal gland, skeletal muscles, or salivary gland. No significant blood clot was also observed. Rare medullary interstitial aggregates of lymphocytes, plasma cells, and macrophages were observed in the kidney, whereas the heart showed the abundance of rare mononuclear aggregates in the myocardium. Small numbers of lymphocytes were found to be present within the lamina propria and are transmigrating through the mucosa. There were rare lymphocytes and plasma cells present within the lamina propria in pyloric stomach. There were rare foci of mineralization present in the tubules admixed with rare lymphocytes and plasma cells in the prostate. Colon appeared to have moderate numbers of lymphocytes and plasma cells admixed with rare eosinophils within the lamina propria. A focal aggregate of mononuclear cells (glial cells) was present within the cortical white matter of the brain. Multiple secondary lymphoid follicles were present in the right popliteal lymph node with macrophages containing dark granular pigment (carbon) and hemorrhages (local drainage). Multiple secondary lymphoid follicles were found to be present in the left popliteal lymph node. Macrophages contained green globular pigment (hemosiderin). Moderate numbers of lymphocytes and plasma cells are present in the conjunctiva (eye). Microscopic diagnosis showed multifocal mild acute hemorrhages with atelectasis in the lung, mild vacuolar degeneration in the liver, focal mononuclear cell encephalitis in the brain, and mild chronic tracheitis in the trachea. Focal encephalitis is always considered important with drug-treated animals. A cause was not observed in these samples. No parasite or fungus was present in these sections. Hemorrhages in the lungs were secondary to intracardiac euthanasia solution. Mild chronic tracheitis and conjunctivitis were likely incidental findings. Mild hepatic vacuolar degeneration was also considered incidental, but an association

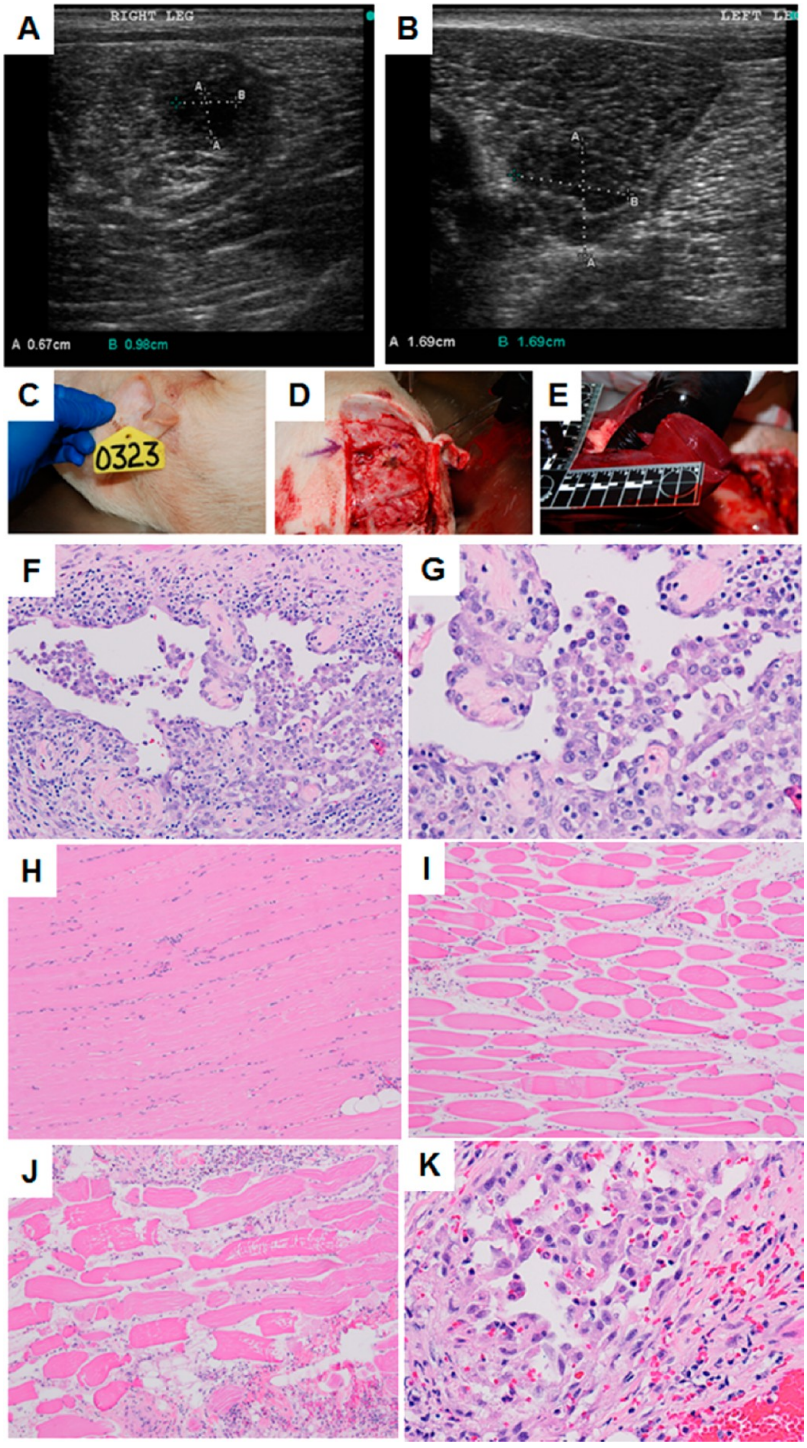


**Figure 12. Representative US images of abnormal tissue growth in the (A) right and (B) left thigh of a transgenic pig. Representative necropsy images: (C) animal identification tag; (D) surgery at the site of US exposure; (E) gross pathology of liver tissue. Histopathological images: (F) neoplastic cells in the tumor from the left thigh showing lining vascular channels and caverns (20×), (G) neoplastic cells in the tumor from the right thigh showing lining vascular channels and caverns (40×), (H) skeletal muscle bundles not treated with thermal ablation (10×), (I) skeletal muscle fibers treated with thermal ablation exhibiting sarcoplasmic hyalinization, loss of striation, cell shrinkage, and increased endomysial space (10×), (J) skeletal muscle fibers treated with thermal ablation exhibiting sarcoplasmic hyalinization, loss of striation, cell shrinkage, sarcoplasmic fragmentation, and increased endomysial space (10×), and (K) neoplastic cells in the tumor from the right thigh exhibiting mild cytoplasmic swelling and vacuolation, indicating vacuolar degeneration from the treatment (40×).**

with the drug should be ruled out. Further in-depth studies will be necessary to confirm these preliminary findings.

**Differential Gene Expression from Swine Liver Tissue.** Therapeutic potential of PBNB through RXR inhibition requires regulation and expression of RXR genes. In addition to

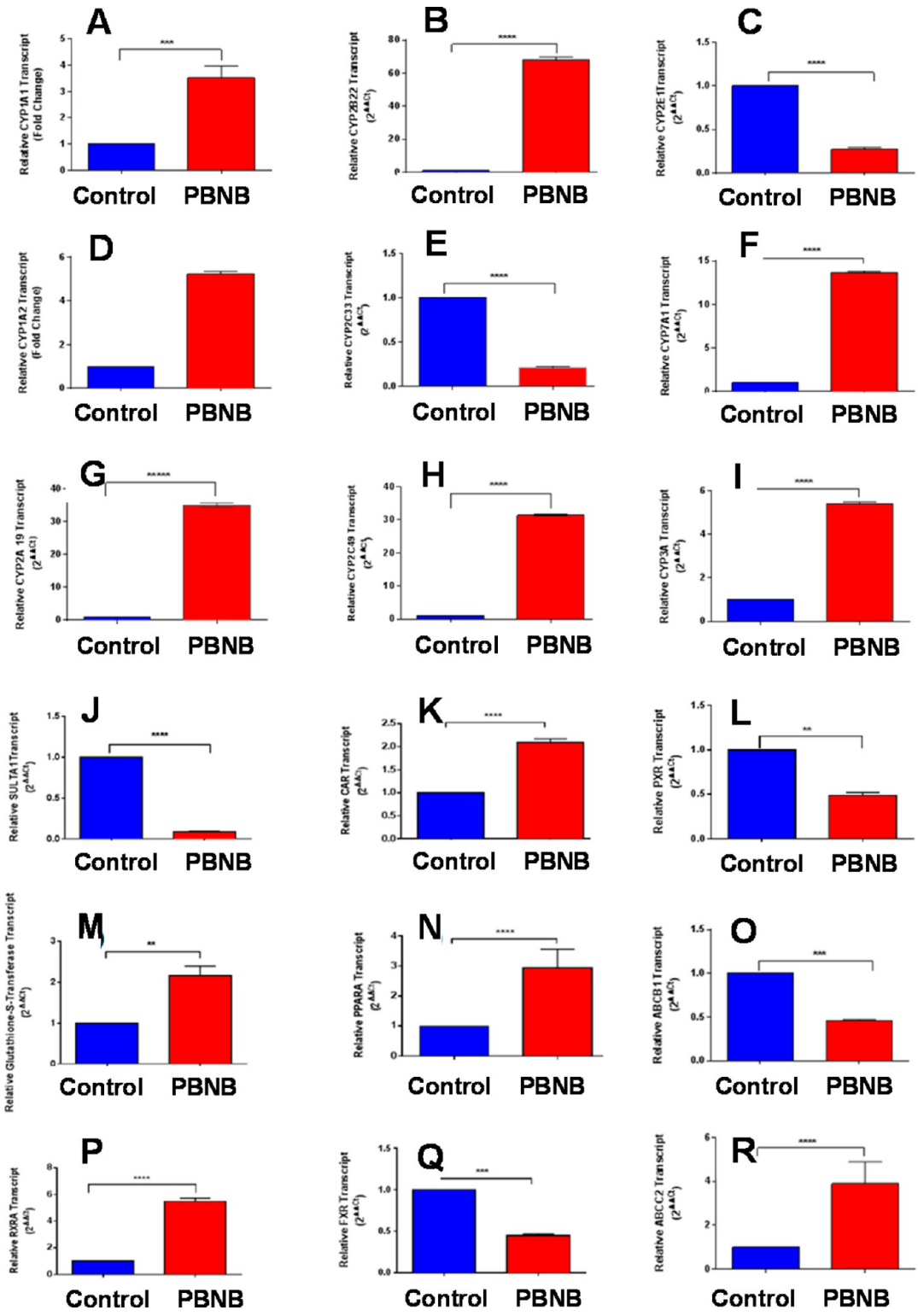


**Figure 13. Differential gene expression studied on genes that might be involved in drug metabolism, regulation, and transport in swine liver tissue. Relative changes in PBNB-treated animals were analyzed for genes (A) CYP1A1, (B) CYP2B22, (C) CYP2E1, (D) CYP1A2, (E) CYP2C33, (F) CYP3A, (G) CYP2A19, (H) CYP2C49, (I) CYP7A1, (J) SULTA1, (K) CAR, (L) PXR, (M) glutathione-S-transferase, (N) PPARα, (O) ABCB1, (P) RXRα, (Q) FXR, and (R) ABCC2. Results indicated that the genes CYP2E1 (C), CYP2C33 (E), SULTA1 (J), FXR (Q), PXR (L), and ABCB1 (O) were down-regulated as expected, and other genes revealed 3−70-fold up-regulation in various cases.**

this, delivery of PBNB should be able to modulate genes related to metabolic pathways involved in phase I and phase II of drug metabolism through the liver. Toward this, differential gene expression studies were performed on genes that might be involved in drug metabolism, regulation, and transport. Toward this, we

identified genes responsive to the treatment of PBNB, including orphan nuclear receptors (regulators), RXRα, CAR, PPARα, FXR, PXR, genes involved in phase I drug metabolism (oxidation reactions), such as CYP1A1, CYP1A2, CYP2A19, CYP2B22, CYP2C33, CYP2C49, CYP2E1, CYP3A, and CYP7A1, genes involved in phase II drug metabolism (conjugation reactions) such as glutathione-S-transferase, SULTA1, and transporters such as ABCB1 and ABCC2. Results indicated that the CYP2E1, CYP2C33, SULTA1, transporters, FXR, PXR, and ABCB1 genes were down-regulated as expected, and other genes revealed 3−70-fold up-regulation in various cases (Figure 13). It clearly confirms the involvement of PBNB through RXR and other gene cascade pathways of swine liver.

## CONCLUSIONS

We successfully demonstrated the integration of a cavitation/sonoporation technique with a unique prodrug nanobubble construct to enhance tissue penetration and ablation by thermal effects of ultrasound. Bexarotene, a known FDA-cleared anticancer agent, was repurposed and repackaged into a sensitive nanobubble form for the application with US-mediated ablation therapy. Molecular dynamics simulations, dynamic light scattering, ζ-potential, Raman spectroscopy, and electron microscopic analysis were used to analyze these particles and response under US exposure. Molecular dynamics simulation studies and free energy data confirmed that PBNB ruptures in response to US, directing a favorable cell entry of pro-bexarotene. However, at this stage, it was inconclusive whether PBNB interacts with cells *via* fusion with the cell bilayer. An in-depth molecular dynamics simulation study is out of scope and will be reported in the near future. Combined therapy using PBNB with catheter-based high-intensity ultrasound was used to demonstrate the applicability in porcine *in vivo* liver. Histopathology analysis of tissue treated with combined therapy showed enhanced tissue damage when compared with tissue treated with only high-intensity ultrasound. The presence of nano-chemotherapeutics in prodrug form showed cell bursting due to cavitation effects from bubble bursting. Bubbles in cytoplasm were observed from histopathology analysis in tissue treated with ultrasound in the presence of either nanobubbles or PBNB. Such results show the significance of the combined therapy, where damage occurs from the cellular to the tissue level. This may be due to the fact that the thermal dose and cavitation sensitizes the cells to enhance chemotherapeutic effects.

A liver cancer model was not available in a large animal, which would allow us to test our therapeutic regime. An improvised approach was taken where hepatocytes were isolated from transgenic oncopig and able to produce a tumor in a mouse liver, as positively confirmed by histopathology of HCC nature. These transformed hepatocytes were used for *in vitro* assessment of drug activity as either a free small molecule or PBNB, which resulted in a significant cellular regression and improved $IC_{50}$ by 2−2.5-fold in the case of PBNB. Since we were dealing with the combination therapeutic approach and just not the drug effect, it was critical to test it in a large animal preclinical model that allows for the use of the flexible ablation catheter. The transgenic tumor pig was developed,[49] and the tumor development was monitored by using US imaging, and after the administration of drug and ablation therapy, the destruction of the tumor was followed by histopathological analyses. Detailed analyses showed that while untreated tissues appeared histopathologically normal, in the case of ablated animals, sign of sarcoplasmic hyalinization, loss of striation, cell shrinkage, and increased endomysial space were predominant. For the drug-treated tissue, the vacuolar degeneration was obvious, presumably due to the effect from the administration of the drug. Differential gene expression indicated that various genes were responsive to the treatment of PBNB, including orphan nuclear receptors (regulators), RXRα, CAR, PPARα, FXR, PXR, and genes involved in phase I and phase II drug metabolism. It clearly confirms the involvement of PBNB through RXR and other gene cascade pathways of swine liver. In short, these results, together with our *in vitro* optimization study and *ex vivo* and *in vivo* liver model, demonstrated the combinatorial treatment approach for this disease, which is normally difficult to intervene and requires complete surgical intervention.

## EXPERIMENTAL SECTION

**Materials and Methods.** Bexarotene was obtained from Sigma-Aldrich, Inc. (St. Louis, MO), while Lyso-PC was purchased from Avanti Polar Lipids (Birmingham, AL). The hydrodynamic diameter was measured on a Malvern Zetasizer machine equipped with 633 nm laser. ζ-Potential measurement was performed on a Malvern Zetasizer instrument, from the MRL facility, UIUC. The TEM images were acquired on a JEOL 2100 cryo-TEM machine and imaged by a Gatan UltraScan 2k × 2k CCD. The XRD data were collected on a Siemens-Bruker D5000 diffractometer and analyzed using Jade software X-ray analysis. The Raman experiments were performed using a Renishaw mircoPL/Raman microscope system. A 633 nm HeNe laser (with a beam width of 1.12 μm) was used to excite the analytes (50× objective, NA = 0.45). The power used for the experiments was 2 mW. All the data were recorded with WiRE3.2 software. All simulations were carried out with NAMD 2.9 (http://www.ks.uiuc.edu/Research/namd/2.9/ug/). TheraVision ultrasound ablation system (Acoustic MedSystems, IL) was used to drive the flat square ultrasonic transducer. MTT reduction assay was ended by performing an absorption assay on a plate reader (Synergy HT, Bio-Tek). Bright-field imaging was performed on a DMI3000 B microscope, Leica Microsystems, Buffalo Grove, IL.

Nanomedicine approaches have been extensively explored as anticancer strategies[64] and for diagnostics.[65] In this

nanomedicinal approach, bexarotene was repurposed as a lipase labile prodrug. Pro-bexarotene NPs were prepared by a membrane formation method. Prepared membranes were hydrated, followed by vortexing and bath sonication to prepare pro-bexarotene NPs. $C_3F_8$ gas was passed through a prepared colloidal suspension and air above the suspension, generating PBNB. Similarly, the lipid Lyso-PC was used to generate NBs as control nanobubbles. Average hydrodynamic diameter distributions for PBNB and NB formulations before and after exposure to optimized ultrasonication (PBNB+US and NB+US) were determined using a Malvern Zetasizer nanoseries, Nano ZS90, at various time points of 0−120 h. $\zeta$-Potential values for the formulations before and after exposure to optimized ultrasonication (PBNB+US and NB+US) were determined with a nanoseries Malvern Zetasizer $\zeta$-potential analyzer, while measurements of $\zeta$ were reproducible to within $\pm 5$. The morphological investigations on pro-bexarotene NPs and PBNBs were performed by transmission electron microscopy using negative staining with uranyl acetate.

The ordered behavior of pro-bexarotene NPs, PBNB, and PBNB+US was determined by X-ray diffraction measurement on a Siemens-Bruker D5000 diffractometer. Scans were performed for a $2\theta$ range of 2 to 50. Raman spectroscopic measurements were performed to reveal unique Raman scattering patterns of PBNB and NB before and after US exposure and compared with powdered samples of pro-bexarotene, bexarotene, and lipid Lyso-PC. The Raman experiments were performed using a Renishaw microPL/Raman microscope system. A 633 nm HeNe laser (with a beam width of 1.12 $\mu$m) was used to excite the analytes (50× objective, NA = 0.45). The power used for the experiments was 2 mW. All the data were recorded with WiRE3.2 software. The fate of PBNBs after US exposure was simulated with NAMD 2.9 (http://www.ks.uiuc.edu/Research/namd/2.9/ug/). All simulations were performed in the NPT ensemble, where pressure was kept constant at 1 atm by the Langevin piston method.

**Preparation of PBNBs.** Pro-bexarotene (1 mg/mL) was dissolved in $CHCl_3$/MeOH (4:1) for membrane formation under a reduced pressure rotary evaporator at 40 °C for 10 min. Prepared membranes were kept under vacuum to remove traces of organic solvents. Prepared membranes were first hydrated with hot water (~60 °C) for 20 min, followed by keeping at 4 °C for >12 h. At the end of hydration process, membranes were heated at 60 °C for 10 min, followed by 5 min vortexing and 5 min bath sonication. The above cycle was repeated three times. Prepared nanoparticles were characterized by dynamic light scattering and $\zeta$-potential measurement. $C_3F_8$ gas was passed through a prepared soy lecithin nanoparticle colloidal suspension for 3 min. Air above the suspension in the preparation tube was replaced with $C_3F_8$ by continuous flow for the next 1 min. Prepared nanobubbles were characterized by dynamic light scattering and $\zeta$-potential measurement.

**Dynamic Light Scattering.** Average hydrodynamic diameter distributions for PBNB and NB formulations before and after exposure to optimized ultrasonication (PBNB+US and NB+US) were determined using a Malvern Zetasizer nanoseries, Nano ZS90. Scattered light was collected at a fixed angle of 90°. A photomultiplier aperture of 400 mm was used, and the incident laser power was adjusted to obtain a photon counting rate between 200 and 300 kcps. Only measurements for which the measured and calculated baselines of the intensity autocorrelation function agreed to within +0.1% were used to calculate nanoparticle hydrodynamic diameter values. The measurements for the particles were made at 0, 24, 48, 72, 96, and 120 h after synthesis to evaluate the stability. All determinations were made in multiples of five consecutive measurements.

**$\zeta$-Potential Determination.** $\zeta$-Potential ($\zeta$) values for the PBNB and NB formulations before and after exposure to optimized ultrasonication (PBNB+US and NB+US) were determined with a nanoseries Malvern Zetasizer $\zeta$-potential analyzer. Measurements were made following dialysis (MWCO 20 kDa dialysis tubing, Spectrum Laboratories, Rancho Dominguez, CA) of nanoparticle suspensions into water. Data were acquired in the phase analysis light scattering mode following solution equilibration at 25 °C. Calculation of $\zeta$ from the measured nanoparticle electrophoretic mobility ($\mu$) employed the Smoluchowski equation: $\mu = \varepsilon\zeta/\eta$, where $\varepsilon$ and $\eta$ are the dielectric constant and the absolute viscosity of the medium, respectively. Measurements of $\zeta$ were reproducible to within $\pm 5$ mV of the mean value given by 20 determinations of 10 data accumulations.

**Transmission Electron Microscopy.** TEM was performed on pro-bexarotene NPs and PBNBs to evaluate their morphologies. Imaging was performed on samples prepared on copper grids that were coated with a Formvar plastic and then coated with carbon for stability, followed by negative staining with uranyl acetate.

**X-ray Diffraction Studies.** The ordered behavior of pro-bexarotene NPs, PBNB, and PBNB+US was determined by X-ray diffraction measurement. The aqueous aggregates of each formulation were placed on a precleaned glass plate, which, upon air drying, afforded a thin film of the formulations on the glass plate. XRD of an individual cast film was performed using the reflection method with a Siemens-Bruker D5000 diffractometer. The X-ray beam was generated with a Cu anode, and the Cu K$\alpha$ beam of wavelength of 1.5418 Å was used for the experiments. Scans were performed for a $2\theta$ range of 2 to 50.

**Molecular Dynamics Simulations.** All simulations were carried out with NAMD 2.9 (http://www.ks.uiuc.edu/Research/namd/2.9/ug/).[54] To ensure statistics, 20 independent simulations were performed. Prodrug insertion into the membrane was observed in all simulations. Fifteen simulations were terminated once the insertion was observed, and five of the simulations were performed up to 400 ns to study prodrug-in-membrane stability. Parameters were generated using the CHARMM general force field (CGenFF)[56] for bexarotene. CHARMM (c36) force field[57] was applied for the Lyso-PC and the membrane POPC lipids. A modified TIP3P water model[58] in the CHARMM force field was used. Particle-mesh Ewald[59] was used for long-range electrostatic interactions. The r-RESPA multiple time-step integrator[60] was applied with time steps of 2 and 4 fs for short-range nonbonded and long-range electrostatic interactions, respectively. The SETTLE algorithm[61] maintained water rigid geometry, while RATTLE[62] constrained the length of covalent hydrogen bonds. Temperature was set to 300 K for all systems by a Langevin thermostat. All simulations were performed in the NPT ensemble, where pressure was kept constant at 1 atm by the Langevin piston method.[55]

The membrane insertion potential of mean force (PMF) of bexarotene as a part of the prodrug is compared with bexarotene as an independent molecule. Umbrella sampling simulations have been performed to calculate the free energies. Two bexarotene/pro-bexarotene molecules were placed in the system, one at the membrane center and one 52 Å away from the membrane center (outside of the membrane), and thus two PMFs were obtained from a single calculation. Umbrella simulations along the membrane normal at a 1 Å interval were performed for 10 ns each, with the umbrella potentials only on the center of mass of the bexarotene group. The resulting distributions of the bexarotene group were obtained, and the PMFs were calculated based on the distributions *via* the weighted histogram analysis method (WHAM).[63] The PMFs from the two molecules, one in the membrane and one outside, were then averaged to obtained the final PMF, while their difference gave the error estimation.

**Cell Culture.** HepG2 cells were cultured with Eagle's minimum essential medium (EMEM; Sigma) with 10% fetal bovine serum (FBS) and 1× penicillin-streptomycin in T25/T75 culture flasks (Cellstar; Germany) and incubated at 37 °C in a 99% humidified atmosphere containing 5% $CO_2$. Cells were regularly passaged by trypsinization with 0.1% trypsin (EDTA 0.02%, dextrose 0.05%, and trypsin 0.1%) in DPBS (pH 7.4). Nonsynchronized cells were used for all experiments.

***In Vitro* Treatments.** Our preliminary *in vitro* results were obtained using PBNB with pro-bexarotene to investigate the synergistic effects of ultrasound and chemotherapy on HepG2 cells. During the ultrasound experiment, the cell plates were filled with PBS (pH 7.4), covered by a MicroAmp optical adhesive film (Applied Biosystems, Foster City, CA) to act as an acoustic window, and placed inverted in a tank of degassed water.

The optical adhesive film also prevented the solution in the wells from mixing with the water bath. The PBS solution had PBNBs and NBs based on the respective control and treatment configuration. A rectangular flat ultrasonic transducer with a center frequency of 2.4 MHz was used to expose the cell at the surface of each well for 2 min duration at an acoustic power of 10 W and a pulse rate of 0.5 Hz.

HepG2 (p53 wild-type) human HCC tumor cells were obtained from American Type Culture Collection (Rockville, MD) and cultured in RPMI 1640 containing 10% FBS and human insulin (0.01 mg/mL) at the ambient condition of 5% $CO_2$, 99% humidity, and a temperature of 37 °C. HepG2 cells were cultured in ambient conditions prescribed by ATCC, and nonsynchronized cells were used for all experiments. Experimental conditions were optimized to achieve maximum cell growth inhibition. Initially, growth inhibitory effects of US exposures were investigated in 96-well plates by incubating the cells with 60−1.875 $\mu$M of bexarotene, pro-bexarotene, PBNB, and NB at 48, 72, and 96 h time points to find the optimum concentration and $IC_{50}$. Second, PBNB and NB formulations were used for optimization of parameters of US exposures to achieve the maximum as described above. Six-well plates were plated with cells and treated with PBNB and NB formulations for 2 min while exposed to US.

In another set of experiments, cells were treated with PBNB at various concentrations ranging from 60 to 7.5 $\mu$M for the time period of 2 min while exposed to US with optimal parameters. At the end of the US exposure, concentrations were diluted to 15−1.875 and incubated for 72 h. In all experimental conditions, cells were imaged to investigate the growth density and morphology variations followed by MTT assay. The percentage cell viability was obtained from a plate reader and was calculated using the formula, % viability = $\{[A_{630}$(treated cells) − (background)]/$[A_{630}$(untreated cells) − background]$\} \times 100$.

**MTT Assay.** The % viability of cells treated with bexarotene, pro-bexarotene, PBNB, and NB in HepG2 cells was investigated by using 3-(4,5-dimethylthiazole-2-yl)-2,5-diphenyltetrazolium bromide (MTT). NBs were used as the negative control for all experiments. Primarily, experiments were performed to evaluate the $IC_{50}$ values for various used formulations. Experiment was performed in 96-well plates (Cellstar; Germany) by growing 8000 cells per well 24 h before treatments. Experiments were performed for various concentrations of bexarotene, pro-bexarotene, and PBNB (60, 30, 15, 7.5, 3.75, 1.87, 0.935 $\mu$M) present in free or nanoparticle forms, while the same volume of NB was used as negative controls. Cells were incubated for 48, 72 and 96 h before performing the MTT assay. Second, PBNB and NB formulations were used for optimization of parameters of US exposures to achieve the maximum. Six-well plates were plated with $0.3 \times 10^6$ cells and grew for 24 h before the treatments. Cells were treated with PBNB and NB formulations for 2 min while being exposed to US. After the incubation period, cells were imaged to investigate the growth density and morphology variations. Cells were introduced to MTT and trypan blue assays after 24 h. In another set of experiments, cells ($0.3 \times 10^6$ cells and grew for 24 h before the treatments) were treated with PBNB at various concentrations ranging from 15 to 1.875 $\mu$M and the respective volume of NB. Cells were incubated for a further 72 h after exposure to either optimized US parameters or as such. Cells were initially incubated with a 4× concentration of formulations during US while incubated for 72 h at 1× concentrations. After the incubation period, cells were imaged to investigate the growth density and morphology variations. Cells were further treated with MTT as 200 $\mu$L (5 mg/mL) per well and further incubated for 4.5 h. At the end of the incubation, the entire medium was removed from wells and 2000 $\mu$L of dimethylsulfoxide was added to dissolve the blue-colored formazan crystals. Dissolved crystals were transferred to 96-well plates in 20 wells each. The percentage cell viability was obtained from the plate reader and was calculated using the formula, % viability = $\{[A_{630}$(treated cells) − (background)]/$[A_{630}$(untreated cells) − background]$\} \times 100$.

**Mechanistic Studies of RXR Modulation and Other Biological Interactions for PBNB and Controls.** HepG2 cells ($1.5 \times 10^5$) were cultured in 12-well plates and grown until a plating density of ∼80% was achieved with EMEM containing 10% FBS. Cells were treated with gradually increasing PBNB concentrations (*i.e.*, 6.25, 12.5, 25, and 50 $\mu$M), along with control formulations of NBs. Cells were exposed to therapeutic US as optimized earlier and were allowed to grow for 72 h. At the end of the incubation period, cells were washed with 200 $\mu$L of 3× DPBS to remove traces of serum for better trypsinization followed by collection in 1 mL of 10% FBS containing DMEM. Cells were pelleted by spinning down at 4000 rpm for 5 min at 4 °C. Cells were intermittently vortexed while fixing with 75% ethanol and stored at −20 °C for 12 h. Then cells were spun down at 4000 rpm for 5 min at 4 °C, and pellets were washed thoroughly with DPBS. Cells were suspended in 100 $\mu$L of DPBS and then treated with RNase (10 $\mu$g) for 12 h at 37 °C. Cells were stained with 2 $\mu$g/mL of PI for 30 min at room temperature in the dark before the flow-assisted cell analysis (FACS) was performed and the percentage apoptotic cell population analyzed.

To further probe cellular apoptosis, DNA fragmentation assay was performed on treated cells. Treatments were implemented as described above, only with a change in their harvesting protocol. At the end of the 72 h incubation period, cells were harvested in 1 mL of 10% FBS containing culture medium and washed with 1 mL of DPBS for two times. Harvested cells were spun at 1000 rpm for 2 min to obtain cell pellets, which were incubated with 400 $\mu$L of lysis buffer (Thermo Scientific) at 65 °C. Lysed cell suspensions were mixed thoroughly with 400 $\mu$L of $CHCl_3$ and spun at 12000 rpm at 4 °C for 5 min after intermittent mixing. The water layer was collected, and a solution of 100 $\mu$L of NaCl with 800 $\mu$L of chilled ethanol was added to it before the mixture was maintained at −20 °C overnight. Suspensions were pelleted down at 12000 rpm at 4 °C for 20 min and washed with 75% ethanol. DNA pellets were air-dried before being dissolved in TE buffer at pH 7.4. Extracted genomic DNA was run on 2% agarose gel using 1× TAE buffer at 100 V for 30 min.

**Interaction of Bexarotene with Duplex Plasmid DNA and the Effect of Its Prodrug and Nanobubble form on Electrophoretic Mobility.** Propidium iodide staining and DNA laddering assays established the probable induction of apoptosis *via* US-mediated internalization of PBNB. To negate the chemical degradation of genomic DNA by PBNB and its chemical ingredients, gel electrophoresis was performed on plasmid DNA incubated with various formulations. A pBR322 vector DNA (pDNA; New England Biolabs, Ipswich, MA) was used (200−500 ng/cocktail) to prepare various mixtures containing bexarotene, pro-bexarotene, PBNB, and NB. The mixtures were allowed to be incubated at room temperature for 1 h. All incubated samples were loaded on a 1% agarose gel along with unbound pDNA and DNA ladder (0.1−10 kb) and ran at 100 V for 30 min. Finally, gel was stained in 10 $\mu$g/mL ethidium bromide solution in 1× TAE for 5 min and washed in 1× TAE solution for 5 min before being imaged (Universal Hood III, Bio-Rad, Hercules, CA).

**RXR Agonist Assay.** Experiment was performed using INDIGO's panel of RXR reporter assay (Cayman chemicals, INDIGO Biosciences) which utilizes non-human mammalian cells engineered to express human retinoic acid receptor, RXRα. Cells include the luciferase reporter gene functionally linked to a responsive promoter that provides quantification of changes in luciferase expression in treated reporter cells. This quantification provides a sensitive surrogate measure of the changes in RXRα activity. Formulations including bexarotene, pro-bexarotene, and PBNB were used to verify their RXR agonist abilities at concentrations ranging from 50 to 0.5 $\mu$M along with positive control 9-*cis*-retinoic acid supplied with an assay kit at 5 $\mu$M. Cells were treated for 24 h before the luciferase activity was measured. Experiment was performed using the manufacturer's protocol. Luciferase activities were acquired as luminescence using a multiwall plate reader at various time points ranging from 5 to 50 min.

***Ex Vivo* Experiments and Optimization of Catheter-Based Ultrasonic Exposures.** Freshly excised porcine liver tissue samples were obtained immediately postnecropsy from the Meat Science Laboratory at the University of Illinois at Urbana—Champaign. The experiment was conducted within 30 min from extracting the tissue from the animal. Following treatment, the tissue was dissected for gross pathology and visual inspection. After being

dissected, the tissue was submerged into triphenyltetrazolium chloride (TTC) for viability staining. The TTC made the treated region appear in a different color than the normal tissue for easier visual identification of the thermal treatment region.

The catheter-based ultrasound interstitial applicator with two element tubular PZT transducers was used in the experiment (Figure S7). The transducers were mounted on a hollow supporting tube. The PZT transducers were 10 mm long with 1.5 mm outer diameter. The applicator was inserted into the tissue for treatment using a 13 gauge implant catheter. Degassed water was circulated through the applicator and the catheter to cool the transducer during ablation. Degassed water was used to minimize the presence of bubbles. Transducers with 360° active zones, as shown in Figure S7B,C, were used for the experiments.

Using electrical impedance and radiation force balance measurements, the center frequency and efficiency of each transducer were determined. The center frequency of each individual transducer was used to excite the respective transducer to maximize energy output. Continuous wave operation was used to excite the transducers. Typically, the transducer center frequency ranged from 6.5 to 7.5 MHz with an acoustic efficiency of 50−60%. Here, the transducer closer to the tip of the catheter was referred to as Tx1 and the second transducer as Tx2, as shown in Figure S7.

A multichannel generator/amplifier/controller system (TheraVision, Acoustic MedSystems Inc., Savoy, IL), with independent RF power and frequency control configured to supply high power to the US applicators, was used in the experiment (Figure S7D). Real-time ultrasound imaging was acquired using a SonixTouch (Ultrasonix, Canada) clinical ultrasound imaging system to inject the nanomedicine into the excised tissue.

**Optimization of Ultrasonic Exposures.** *In vitro* treatments of PBNB and NB formulations before and after exposure to optimized ultrasonication (PBNB+US and NB+US) were performed for optimization of plated cell density, growth span, and US exposure power and time followed by concentration and incubation of formulations. Initially, 6-well plates were plated with $3 \times 10^5$ cells for 24 h before the cells were incubated with various concentrations of PBNB and NBs. During the ultrasound experiment, the cell plates were filled with PBS (pH 7.4), covered by a MicroAmp optical adhesive film (Applied Biosystems, Foster City, CA) to act as an acoustic window, and placed inverted in a tank of degassed water. The optical adhesive film also prevented the solution in the wells from mixing with the water bath.

**US Setup and Optimization.** TheraVision ultrasound ablation system (Acoustic MedSystems, IL) was used to drive the flat square ultrasonic transducer (Figure S1). The transducer was held positioned such that the acoustic beam was centered at each well in the 12-well plate. A pulse rate of 0.5 Hz was used for all experiments (Figure S1B). The transducer was held stationary, and the plate was moved to expose each separate well containing cells for the respective configurations in the plate. The size of the transducer was 18 mm diagonally (Acoustic MedSystems, IL), which was slightly smaller than the diameter of each well (22 mm) such that each well is exposed by the collimated acoustic beam. Degassed water at 37 °C was used for all experiments. The RF generator in the TheraVision system uses a sophisticated circuit design that minimizes changes in pressure amplitude and frequency settings. Each well was exposed for 2 min. During the ultrasound experiment, the plates were covered by a MicroAmp optical adhesive film (Applied Biosystems, Foster City, CA) to act as an acoustic window and placed inverted in a tank of degassed water (Figure S1a). The optical adhesive film prevented the solution in the wells from mixing with the water bath and acted as an acoustic window. The plate was inverted so that the PBNB would float and be near the cell surface. Typically, the four farthest corner wells in a 12-well plate were used for the ultrasound experiment to avoid any ultrasound exposure to the adjacent wells.

**High-Intensity Ultrasound Therapy.** The Acoustx catheter-based ultrasound interstitial applicator with two element tubular PZT transducers was used in the experiment (Figure S7) for therapeutic ultrasound delivery. Each transducer was 10 mm long with 1.5 mm outer diameter and mounted on a polyamide support structure. The applicator was inserted into a 13 gauge implant catheter, which was inserted into the target liver tissue. Degassed water was circulated through the applicator and the catheter to cool the transducers during ablation. Use of degassed water minimized the presence of bubbles. Transducers with 360° angular active zones as shown in Figure 1B,C were used for the experiments.

The center frequency and efficiency of each transducer were determined using electrical impedance and radiation force balance measurements. The center frequency of each individual transducer was used to excite the respective element to maximize energy output. Continuous wave operation was used for energy delivery. Typically, transducer center frequency ranged from 6.5 to 7.5 MHz with acoustic efficiency of 50−60%. Here, the transducer closer to the tip of the catheter was referred to as Tx1 and the second transducer as Tx2, as shown in Figure S7.

A multichannel generator/amplifier/controller system (TheraVision, Acoustic MedSystems Inc., Savoy, IL), with independent RF power and frequency control configured to supply high power to the US applicators was used in the experiment (Figure S7D). Real-time US imaging was acquired using SonixTouch (Ultrasonix, Richmond, BC, Canada), a clinical imaging system, to inject the nanomedicine into the tissue.

***In Vivo* Experimental Setup.** The PBNB was injected into the liver tissue under ultrasound image guidance (Figure S8). One milliliter of PBNB solution was injected into the *in vivo* liver tissue. As soon at the needle was extracted from the tissue, the Acoustx catheter and fine needle thermocouples were inserted into the target tissue. The ultrasound experiment started within a few minutes from injecting the PBNB nanomedicine. The release of the PBNB solution from the needle tip was clearly visible in the ultrasound B-mode image (Figure S8b). Ultrasound imaging helped to confirm the injection site of the nanomedicince into the tissue and facilitation of placement of the ultrasound therapy device.

Immediately post-injection of PBNB, the Acoustx applicators and fine needle thermocouples were inserted into the tissue using a custom template (Figure S9). Fine needle thermocouple sensor arrays of type T (Physitemp, NJ) were placed at 5, 10, 15, and 20 mm distances radially from the center of the applicator. Each sensor needle was $100 \pm 2$ mm long and 0.8 mm diameter with 0.1 °C accuracy in temperature measurement. Each fine needle thermocouple included multiple sensors along its length at 0, 10, and 20 mm from the tip of the needle. The tip of the fine needle thermocouple was placed at a depth axially aligned with the center of the distal transducer along its axis such that at least one sensor was placed within the treatment region for each tubular transducer along the axial length of the applicator. Custom insertion templates were used to insert the Acoustx applicators and fine needle thermocouples for thermometry measurement. The custom templates were used to maintain parallel tracks of therapy applicators and fine thermocouple needles during the experiment at specified predetermined radial distances.

The Acoustx ultrasound therapy catheter was inserted into the tissue under 3D tracked ultrasound image guidance (Figure S9A). Ultrasound imaging was acquired using a SonixTouch (Ultrasonix, Richmond, BC, Canada) system, which is an FDA-approved clinical ultrasound system with an L14-5/38 GPS probe. The SonixGPS system built into SonixTouch system was used for tracking. An in-house software architecture was developed to communicate with the hardware, ultrasound imaging, and tracking system. Specifically, the ultrasound imaging and tracking were performed using the PLUS software and Open IGT Link interface in conjunction with AMS custom software. For 3D tracked ultrasound targeting, the EM sensor was inserted into the implant catheter to the distal tip, which was then inserted into the target tissue guided by combined ultrasound imaging with GPS tracking. After the implant catheter was positioned at the treatment location, the EM sensor was removed from the implant catheter and the ultrasound therapy applicator inserted into the implant catheter tip. A custom template (Figure S9) was used to position the applicator and thermocouples. The tracked

imaging screen view of the TheraVision system is shown in Figure S9B, showing the 3D (top) and 2D B-mode (bottom) view of the ultrasound image guidance.

***In Vivo* Experiments.** *In vivo* validation tests were performed in porcine liver tissue using the TheraVision ultrasound ablation system with Acoustx interstitial ultrasound applicators (Acoustic MedSystems (AMS), USA). The experimental protocol was approved by the Institutional Animal Care and Use Committee (IACUC), University of Illinois at Urbana—Champaign, and satisfied all University and National Institutes of Health (NIH) rules for the humane use of laboratory animals. The animal was anesthetized with an intramuscular or intravenous injection of TKX (a combination of 2.5 mL of xylazine (100 mg/mL) and 2.5 mL of ketamine (100 mg/mL) added to a Telazol (50 mg of tiletamine and 50 mg of zolazepam) vial) and administered at a dosage of 2.2 mg/kg of a 50 mg/mL concentration. Following TKX administration, anesthesia was continued by tracheal intubation and maintained at a surgical plane of anesthesia on isoflurane/oxygen (2−4% v/v/2−4 L/min). A ventral midline laparotomy approach was used to expose and access the liver for treatment. A linear array ultrasound imaging probe (L14-5/38, Ultrasonix, Richmond, BC, Canada) was used to image the targeted tissue and locate the desired treatment region. Using ultrasound imaging together with EM tracking system, PBNB nanoparticles were injected using a 23 gauge syringe, and then the catheter was inserted into the liver as per the treatment plan. After treatment, the animals were euthanized per the Guide for the Care and Use of Laboratory Animals and followed approved UI IACUC protocols, using sodium pentobarbitol (fatal plus 10 cc/100 lb IV), and the tissue was harvested for gross and histopathological analysis.

**Differential Gene Expression Studies.** Differential gene expression was studied of RXR and other genes that might be involved in drug metabolism, regulation, and transport by quantitative RT-PCR. Total RNA was isolated from porcine liver tissue using RNeasy mini kit (Qiagen) as per manufacturer's protocol. Reverse transcription of RNA was performed from 1 $\mu$g of RNA in the presence of RNase inhibitor, random hexamer primers (50 ng/$\mu$L), deoxynucleotides (dNTPs, 10 mM), SuperScript III reverse transcriptase (200 U/$\mu$L), and reverse transcriptase buffer in a 20 $\mu$L final reaction volume using the SuperScript III first-strand synthesis system for the RT-PCR kit (Invitrogen). Reverse transcription was performed at 50 °C for 50 min. Relative quantification of the genes involved in phase I and Phase II drug metabolism and transport was performed by using Power SYBR green PCR master mix (2X) (Applied Biosystems) in a Taqman ABI 7900 real-time PCR system (Applied Biosystems). The housekeeping gene GAPDH was used as reference gene for normalization of target genes expressed in porcine liver. The specificity of all primer pairs was checked by melting curves of the amplified products.

**Statistical Analysis.** Statistical significance of differences between control and samples were evaluated using one-way or two-way ANOVA using GraphPad Prizm 5.0 with Bonferroni post-test analysis as applicable. Results were considered statistically significant when the $p$ value was less than 0.05.

*Conflict of Interest:* The authors declare no competing financial interest.

*Supporting Information Available:* The Supporting Information is available free of charge on the ACS Publications website at DOI: 10.1021/acsnano.5b05974.

Synthesis of pro-bexarotene, experimental setup for *in vitro* U.S. studies, Raman spectroscopic details of NB samples, MTT assay experiments, bright-field images of HepG2 cells, experimental setup for *ex vivo* pig liver tissue, temperature profile of the three thermocouples, and location of the applicators and the flexible needles (PDF)
Movies 1−20 (ZIP)

*Acknowledgment.* This work was supported by the University of Illinois at Urbana—Champaign, USA, and was also partially supported by grants to D.P. from Children's Discovery Institute. We acknowledge Paul Neubauer (AMS) for help with the instrumentation setup. The research has been partially supported through grants by the National Institutes of Health (R01-GM067887, 9P41GM104601, U54 GM087519) and by the National Science Foundation (PHY1430124). The authors also acknowledge supercomputer time on Stampede at the Texas Advanced Computing Center (TACC), provided by Grant MCA93S028 from the Extreme Science and Engineering Discovery Environment (XSEDE), which is supported by the National Science Foundation (OCI-1053575). S.K.M., G.G., M.R.G., M.Y., E.M.W., C.R.B., K.V.T., P.S.R., E.C.B, K.S., A.K.D. and D.P. designed and executed all the materials physico-chemical, DFT simulation, biological and US experiments presented here. Z.W. and K.S. designed and executed molecular dynamics simulation studies. S.K.M., G.G., P.S.R., and D.P. wrote the manuscript. All the authors participated in reviewing and editing it. Authors gratefully acknowledge the associate editor Prof. Warren Chan for his suggestion and comments to improve this manuscript.

## REFERENCES AND NOTES

1. Siegel, R.; Naishadham, D.; Jemal, A. Cancer Statistics, 2013. *Ca-Cancer J. Clin.* **2013**, *63*, 11–30.
2. Duvic, M.; Hymes, K.; Heald, P.; Breneman, D.; Martin, A. G.; Myskowski, P.; Crowley, C.; Yocum, R. C. Bexarotene is Effective and Safe for Treatment of Refractory Advanced-Stage Cutaneous T-Cell Lymphoma: Multinational Phase II-III Trial Results. *J. Clin. Oncol.* **2001**, *19*, 2456–2471.
3. Sherman, S. I.; Gopal, J.; Haugen, B. R.; Chiu, A. C.; Whaley, K.; Nowlakha, P.; Duvic, M. Central Hypothyroidism Associated with Retinoid X Receptor-Selective Ligands. *N. Engl. J. Med.* **1999**, *340*, 1075–1079.
4. Szanto, A.; Narkar, V.; Shen, Q.; Uray, I. P.; Davies, P. J. A.; Nagy, L. Retinoid X receptors: X-Ploring their (Patho)-physiological Functions. *Cell Death Differ.* **2004**, *11*, S126–S143.
5. Hoe, A. L.; Royle, G. T.; Taylor, I. Breast Liver Metastases--Incidence, Diagnosis and Outcome. *J. Royal Soc. Med.* **1991**, *84*, 714–716.
6. Okano, K.; Maeba, T.; Ishimura, K.; Karasawa, Y.; Goda, F.; Wakabayashi, H.; Usuki, H.; Maeta, H. Hepatic Resection for Metastatic Tumors from Gastric Cancer. *Ann. Surg.* **2002**, *235*, 86–91.
7. Manfredi, S.; Lepage, C.; Hatem, C.; Coatmeur, O.; Faivre, J.; Bouvier, A. M. Epidemiology and Management of Liver Metastases from Colorectal Cancer. *Ann. Surg.* **2006**, *244*, 254–259.
8. Kagohashi, K.; Satoh, H.; Ishikawa, H.; Ohtsuka, M.; Sekizawa, K. Liver Metastasis at the Time of Initial Diagnosis of Lung Cancer. *Med. Oncol.* **2003**, *20*, 25–28.
9. Shingleton, W. B.; Sewell, P. E., Jr. Cryoablation of Renal Tumours in Patients with Solitary Kidneys. *BJU Int.* **2003**, *92*, 237–239.
10. Bahn, D. K.; Lee, F.; Badalament, R.; Kumar, A.; Greski, J.; Chernick, M. Targeted Cryoablation of the Prostate: 7-Year Outcomes in the Primary Treatment of Prostate Cancer. *Urol.* **2002**, *60*, 3–11.
11. Curley, S. A.; Curley, S. A.; Izzo, F.; Delrio, P.; Ellis, L. M.; Granchi, J.; Vallone, P.; Fiore, F.; Pignata, S.; Daniele, B.; et al. Radiofrequency Ablation of Unresectable Primary and Metastatic Hepatic Malignancies: Results in 123 Patients. *Ann. Surg.* **1999**, *230*, 1–8.
12. Goldberg, S. N.; Solbiati, L.; Hahn, P. F.; Cosman, E.; Conrad, J. E.; Fogle, R.; Gazelle, G. S. Large-Volume Tissue Ablation with Radio Frequency by Using a Clustered, Internally Cooled Electrode Technique: Laboratory and Clinical Experience in Liver Metastases. *Radiology* **1998**, *209*, 371–379.
13. Gillams, A. R. The Use of Radiofrequency in Cancer. *Br. J. Cancer* **2005**, *92*, 1825–1829.
14. Decadt, B.; Siriwardena, A. K. Radiofrequency Ablation of Liver Tumours: Systematic Review. *Lancet Oncol.* **2004**, *5*, 550–560.
15. Dong, B. W.; Liang, P.; Yu, X. L.; Zeng, X. Q.; Wang, P. J.; Su, L.; Wang, X. D.; Xin, H.; Li, S. Sonographically Guided Microwave Coagulation Treatment of Liver Cancer: An Experimental and Clinical Study. *AJR, Am. J. Roentgenol.* **1998**, *171*, 449–454.

16. Liang, P.; Dong, B.; Yu, X.; Yu, D.; Wang, Y.; Feng, L.; Xiao, Q. Prognostic Factors for Survival in Patients with Hepatocellular Carcinoma After Percutaneous Microwave Ablation. *Radiology* **2005**, *235*, 299–307.
17. Simon, C. J.; Dupuy, D. E.; Mayo-Smith, W. W. Microwave Ablation: Principles and Applications. *Radiol. Soc. N. Am. Inc.* **2005**, *25*, S69–83.
18. Kennedy, J. E. High-Intensity Focused Ultrasound in the Treatment of Solid Tumours. *Nat. Rev. Cancer* **2005**, *5*, 321–327.
19. Blana, A.; Walter, B.; Rogenhofer, S.; Wieland, W. F. High-Intensity Focused Ultrasound for the Treatment of Localized Prostate Cancer: 5-Year Experience. *Urol.* **2004**, *63*, 297–300.
20. Blana, A.; Rogenhofer, S.; Ganzer, R.; Lunz, J.-C.; Schostak, M.; Wieland, W. S.; Walter, B. Eight Years' Experience with High-Intensity Focused Ultrasonography for Treatment of Localized Prostate Cancer. *Urol.* **2008**, *72*, 1329–1333.
21. Schlesinger, D.; Benedict, S.; Diederich, C.; Gedroyc, W.; Klibanov, A.; Larner, J. MR-Guided Focused Ultrasound Surgery, Present and Future. *Med. Phys.* **2013**, *40*, 080901.
22. Yang, R.; Reilly, C. R.; Rescorla, F. J. High-Intensity Focused Ultrasound in the Treatment of Experimental Liver Cancer. *Arch. Surg.* **1991**, *126*, 1002–1009.
23. Yang, R.; Reilly, C. R.; Rescorla, F. J.; Faught, P. R.; Sanghvi, N. T.; Fry, F. J.; Franklin, T. D., Jr.; Lumeng, L.; Grosfeld, J. L. Extracorporeal Liver Ablation Using Sonography-Guided High-Intensity Focused Ultrasound. *Invest. Radiol.* **1992**, *27*, 796–803.
24. Madersbacher, S.; Marberger, M. *What Is the Newest Technology in Treating Prostate Cancer? Transrectal High-Intensity Focused Ultrasound*; Mydlo, J. H., Godec, C. J., Eds.; Academic Press, 2003; pp 529−534.
25. ter Haar, G.; Rivens, I.; Chen, L.; Riddler, S. High Intensity Focused Ultrasound for the Treatment of Rat Tumours. *Phys. Med. Biol.* **1991**, *36*, 1495–1501.
26. Prat, F.; Centarti, M.; Sibille, A.; Fadil, F. A. E.; Henry, L.; Chapelon, J. Y.; Cathignol, D. D. Extracorporeal High-Intensity Focused Ultrasound for VX2 Liver Tumors in the Rabbit. *Hepatology* **1995**, *21*, 832–836.
27. Prat, F.; Lafon, C.; de Lima, D. M.; Theilliere, Y.; Fritsch, J.; Pelletier, G.; Buffet, C.; Cathignol, D. Endoscopic Treatment of Cholangiocarcinoma and Carcinoma of the Duodenal Papilla by Intraductal High-Intensity US: Results of a Pilot Study. *Gastrointest. Endosc.* **2002**, *56*, 909–915.
28. Klingler, C.; Margreiter, M.; Marberger, M. New Ablative Treatments for Small Renal masses: HIFU Ablation. *Arch. Esp. Urol.* **2013**, *66*, 79–89.
29. Hynynen, K.; Jolesz, F. A. Demonstration of Potential Noninvasive Ultrasound Brain Therapy Through an Intact Skull. *Ultrasound Med. Biol.* **1998**, *24*, 275–283.
30. Jeanmonod, D.; Werner, B.; Morel, A.; Michels, L.; Zadicario, E.; Schiff, G.; Martin, E. Transcranial Magnetic Resonance Imaging-Guided Focused Ultrasound: Noninvasive Central Lateral Thalamotomy for Chronic Neuropathic Pain. *Neurosurg. Focus* **2012**, *32*, E1.
31. Aptel, F.; Charrel, T.; Lafon, C.; Romano, F.; Chapelon, J.-Y.; Blumen-Ohana, E.; Nordmann, J.-P.; Denis, P. Miniaturized High-Intensity Focused Ultrasound Device in Patients with Glaucoma: A Clinical Pilot Study. *Invest. Ophthalmol. Visual Sci.* **2011**, *52*, 8747–8753.
32. Charrel, T.; Aptel, F.; Birer, A.; Chavrier, F.; Romano, F.; Chapelon, J. Y.; Denis, P.; Lafon, C. Development of a Miniaturized HIFU Device for Glaucoma Treatment with Conformal Coagulation of the Ciliary Bodies. *Ultrasound Med. Biol.* **2011**, *37*, 742–754.
33. Matysiak, J. Evaluation of Electronic, Lipophilic and Membrane Affinity Effects on Antiproliferative Activity of 5-Substituted-2-(2,4-dihydroxyphenyl)-1,3,4-Thiadiazoles Against Various Human Cancer Cells. *Eur. J. Med. Chem.* **2007**, *42*, 940–947.
34. Schon, U.; Antel, J.; Bruckner, R.; Messinger, J.; Franke, R.; Gruska, A. Synthesis, Pharmacological Characterization, and Quantitative Structure-Activity Relationship Analyses of 3,7,9,9-Tetraalkylbispidines: Derivatives with Specific Bradycardic Activity. *J. Med. Chem.* **1998**, *41*, 318–331.
35. Banavath, H. N.; Sharma, O. P.; Kumar, M. S.; Baskaran, R. Identification of Novel Tyrosine Kinase Inhibitors for Drug Resistant T315I Mutant BCR-ABL: A Virtual Screening and Molecular Dynamics Simulations Study. *Sci. Rep.* **2014**, *4*, 6948.
36. Raya, A.; Barrientos-Salcedo, C.; Rubio-Póo, C.; Soriano-Correa, C. Electronic Structure Evaluation Through Quantum Chemical Descriptors of 17$\beta$-aminoestrogens with an Anticoagulant Effect. *Eur. J. Med. Chem.* **2011**, *46*, 2463–2468.
37. Zheng, Y.; Zheng, M.; Ling, X.; Liu, Y.; Xue, Y.; An, L.; Gu, N.; Jin, M. Design, Synthesis, Quantum Chemical Studies and Biological Activity Evaluation of Pyrazole−Benzimidazole Derivatives as Potent Aurora A/B Kinase Inhibitors. *Bioorg. Med. Chem. Lett.* **2013**, *23*, 3523–3530.
38. Magoulas, G. E.; Bariamis, S. E.; Athanassopoulos, C. M.; Haskopoulos, A.; Dedes, P. G.; Krokidis, M. G.; Karamanos, N. K.; Kletsas, D.; Papaioannou, D.; Maroulis, G. Syntheses, Antiproliferative Activity and Theoretical Characterization of Acitretin-Type Retinoids with Changes in the Lipophilic Part. *Eur. J. Med. Chem.* **2011**, *46*, 721–737.
39. Bhattacharjee, A. K.; Karle, J. M. Functional Correlation of Molecular Electronic Properties with Potency of Synthetic Carbinolamines Antimalarial Agents. *Bioorg. Med. Chem.* **1998**, *6*, 1927–1933.
40. Kadam, R. U.; Chavan, A.; Roy, N. Pharmacophoric Features of Pseudomonas aeruginosa Deacetylase LpxC Inhibitors: An Electronic and Structural Analysis. *Bioorg. Med. Chem. Lett.* **2007**, *17*, 861–868.
41. Jentzsch, A. V.; Hennig, A.; Mareda, J.; Matile, S. Synthetic Ion Transporters that Work with Anion-$\pi$ Interactions, Halogen Bonds, and Anion-Macrodipole Interactions. *Acc. Chem. Res.* **2013**, *46*, 2791–2800.
42. Hansch, C.; Steinmetz, W. E.; Leo, A. J.; Mekapati, S. B.; Kurup, A.; Hoekman, D. On the Role of Polarizability in Chemical-Biological Interactions. *J. Chem. Inf. Model.* **2003**, *43*, 120–125.
43. Karelson, M.; Lobanov, V. S. Quantum-Chemical Descriptors in QSAR/QSPR Studies. *Chem. Rev.* **1996**, *96*, 1027–1043.
44. Misra, S. K.; Naz, S.; Kondaiah, P.; Bhattacharya, S. A Cationic Cholesterol Based Nanocarrier for the Delivery of p53-EGFP-C3 Plasmid to Cancer Cells. *Biomaterials* **2014**, *35*, 1334–1346.
45. Yin, T.; Wang, P.; Zheng, R.; Zheng, B.; Cheng, D.; Zhang, X.; Shuai, X. Nanobubbles for Enhanced Ultrasound Imaging of Tumors. *Int. J. Nanomed.* **2012**, *7*, 895–904.
46. MacCallum, J. L.; Bennett, W. F.; Tieleman, D. P. Distribution of Amino Acids in a Lipid Bilayer from Computer Simulations. *Biophys. J.* **2008**, *94*, 3393–3404.
47. Ghoshal, G.; Heffter, T.; Williams, E.; Bromfield, C.; Salgaonkar, V.; Rund, L.; Ehrhardt, J. M.; Diederich, C. J.; Burdette, E. C. *In Situ* Treatment of Liver Using Catheter Based Therapeutic Ultrasound with Combined Imaging and GPS Tracking. *Proc. SPIE* **2013**, 10.1117/12.2008258.
48. Yarmolenko, P. S.; Moon, E. J.; Landon, C.; Manzoor, A.; Hochman, D. W.; Viglianti, B. L.; Dewhirst, M. W. Thresholds for Thermal Damage to Normal Tissues: An Update. *Int. J. Hyperthermia* **2011**, *27*, 320–343.
49. Schook, L. B.; Collares, T. V.; Hu, W.; Liang, Y.; Rodrigues, F. M.; Rund, L. A.; Schachtschneider, K. M.; Seixas, F. K.; Singh, K.; Wells, K. D.; et al. A Genetic Porcine Model of Cancer. *PLoS One* **2015**, *10*, e0128864.
50. Rieke, V.; Pauly, K. B. M R Thermometry. *J. Mag. Reson. Imag.* **2008**, *27*, 376–390.
51. Lepetit-Coiffé, M.; Laumonier, H.; Seror, O.; Quesson, B.; Sesay, M.-B.; Moonen, C. T. W.; Grenier, N.; Trillaud, H. Real-Time Monitoring of Radiofrequency Ablation of Liver Tumors Using Thermal-Dose Calculation by MR Temperature Imaging: Initial Results in Nine Patients, Including Follow-Up. *Eur. Radiol.* **2010**, *20*, 193–201.
52. Rempp, H.; Hoffmann, R.; Roland, J.; Pereira, P.; Schick, F.; Claussen, C.; Clasen, S.; Tübingen, D. E.; Erlangen, D. E.;

Heilbronn, D. E. MR Temperature Mapping at the Radiofrequency Ablation of Liver Tumors: Correlation Between Temperature Data and the Ablation Zone. Presented at the Deutscher Röntgenkongress 2012 (Hamburg), **2013**; DOI: 10.1594/ecr2013/C-0114.
53. He, X.; McGee, S.; Coad, J. E.; Schmidlin, F.; Iaizzo, P. A.; Swanlund, D. J.; Kluge, S.; Rudie, E.; Bischof, J. C. Investigation of the Thermal and Tissue Injury Behaviour in Microwave Thermal Therapy Using a Porcine Kidney Model. *Int. J. Hyperthermia* **2004**, *20*, 567–593.
54. Phillips, J. C.; Braun, R.; Wang, W.; Gumbart, J.; Tajkhorshid, E.; Villa, E.; Chipot, C.; Skeel, R. D.; Kalé, L.; Schulten, K. Scalable Molecular Dynamics with NAMD. *J. Comput. Chem.* **2005**, *26*, 1781–180.
55. Feller, S. E.; Zhang, Y. H.; Pastor, R. W.; Brooks, B. R. Constant Pressure Molecular Dynamics Simulation: The Langevin Piston Method. *J. Chem. Phys.* **1995**, *103*, 4613–4621.
56. Vanommeslaeghe, K.; Hatcher, E.; Acharya, C.; Kundu, S.; Zhong, S.; Shim, J.; Darian, E.; Guvench, O.; Lopes, P.; Vorobyov, I.; et al. CHARMM General Force Field: A Force Field for Drug-Like Molecules Compatible with the CHARMM All-Atom Additive Biological Force Fields. *J. Comput. Chem.* **2010**, *31*, 671–690.
57. Klauda, J. B.; Venable, R. M.; Freites, J. A.; O'Connor, J. W.; Tobias, D. J.; Mondragon-Ramirez, C.; Vorobyov, I.; MacKerell, A. D., Jr.; Pastor, R. W. Update of the CHARMM All-Atom Additive Force Field for Lipids: Validation on Six Lipid Types. *J. Phys. Chem. B* **2010**, *114*, 7830–7843.
58. MacKerell, A. D., Jr.; Bashford, D.; Bellott, M.; Dunbrack, R. L., Jr.; Evanseck, J. D.; Field, M. J.; Fischer, S.; Gao, J.; Guo, H.; Ha, S.; et al. All-Atom Empirical Potential for Molecular Modeling and Dynamics Studies of Proteins. *J. Phys. Chem. B* **1998**, *102*, 3586–3616.
59. Darden, T.; York, D.; Pedersen, L. G. Particle Mesh Ewald: An N·log(N) Method for Ewald Sums in Large systems. *J. Chem. Phys.* **1993**, *98*, 10089–10092.
60. Tuckerman, M.; Berne, B. J.; Martyna, G. J. Reversible Multiple Time Scale Molecular Dynamics. *J. Chem. Phys.* **1992**, *97*, 1990–2001.
61. Miyamoto, S.; Kollman, P. A. Settle: An Analytical Version of the SHAKE and RATTLE Algorithm for Rigid Water Models. *J. Comput. Chem.* **1992**, *13*, 952–962.
62. Andersen, H. C. Rattle: A "Velocity" Version of the Shake Algorithm for Molecular Dynamics Calculations. *J. Comput. Phys.* **1983**, *52*, 24–34.
63. Grossfield, A. *WHAM: The Weighted Histogram Analysis Method*, version 2.0.9, http://membrane.urmc.rochester.edu/content/wham.
64. Kim, B. Y. S.; Rutka, J. T.; Chan, W. C. W. Nanomedicine. *N. Engl. J. Med.* **2010**, *363*, 2434–2444.
65. Hauck, T. S.; Giri, S.; Gao, Y.; Chan, W. C. W. Nanotechnology Diagnostics for Infectious Diseases Prevalent in Developing Countries. *Adv. Drug Delivery Rev.* **2010**, *62*, 438–448.